The bi-azimuthal scattering distribution of an abyssal hill

Nicholas C. Makris[a] and Chin Swee Chia
Massachusetts Institute of Technology, Cambridge, Massachusetts 02139

Laurie T. Fialkowski
Naval Research Laboratory, Washington, DC 20375

(Received 16 September 1998; revised 15 June 1999; accepted 12 July 1999)

High-resolution bistatic images of a typical abyssal hill on the western flank of the Mid-Atlantic Ridge are made with a low-frequency towed-array system operating remotely at 1/2 convergence zone (~33.3 km) stand-off. Comparison with modeled images, generated from high-resolution supporting bathymetry sampled at 5-m intervals, roughly the wavelength scale, reveals that steep scarps return the strongest echoes because they project the largest area along the acoustic path from the source to receiver. Prominent returns deterministically image scarp morphology when the cross-range axis of the system's resolution footprint runs along the scarp axis. Statistical fluctuations inherent in the scattered field prevent the system from distinguishing smaller-scale anomalies on the scarps, such as canyons and gullies (~100–200 m scale), that would otherwise be resolvable in range, in certain bistatic geometries. The mean bi-azimuthal scattering distributions of the two major scarps on the abyssal hill are *identical* and have strengths equal to the *constant* $-17\,\mathrm{dB}\pm 8\,\mathrm{dB}$. This suggests that long-range reverberation from prominent geomorphological features of the world's mid-ocean ridges can be adequately modeled as Lambertian with albedo $\pi/10^{1.7}$, given supporting bathymetry sampled with sufficient frequency to resolve the projected area of these features. [S0001-4966(99)01911-6]

PACS numbers: 43.30.Hw, 43.30.Pc, 43.30.Gv [DLB]

INTRODUCTION

During the Office of Naval Research (ONR) Main Acoustics Experiment (MAE) of July 1993,[1,2] two research vessels equipped both with vertical source and horizontal receiving arrays made bistatic measurements of scattering from a typical, highly lineated, abyssal hill, referred to as B', on the western flank of the Mid-Atlantic Ridge (MAR).[2] These measurements were made for two primary reasons. The first was to investigate the extent to which an abyssal hill, one of the most commonly occurring bathymetric features of the world's oceans, can be deterministically resolved using a remotely operated bistatic towed-array imaging system. The second was to measure the bi-azimuthal scattering distribution of a typical abyssal hill.

In a previous paper, Ref. 2, it was shown that low-frequency towed-array systems can be used to generate wide-area images of prominent geological features in the deep ocean over hundreds of kilometers in near real-time. The brightest features in these images effectively resolve the shape of steep escarpments (~1 km wide) running along the axis of abyssal hills ($\sim 10\times 40$ km) and other bathymetric highs such as inside corner domes (~10 km diameter).[2] Because the resolution of these images greatly exceeds the roughly 10–20-km resolution of currently available bathymetric maps of the world's oceans, where individual abyssal hills remain indistinguishable, there is real promise that towed-array systems may provide a rapid means of charting previously undiscovered bathymetric highs in the deep ocean.

The first main objective of this work is to experimentally determine the effective resolving power of a towed-array system in remotely imaging deep-ocean bathymetry. To do so, an attempt is made to infer the detailed structure of the major scarps on the B' abyssal hill using MAE's bistatic system at 1/2 convergence zone (CZ) stand-off. Since the cross-range resolution of the system (~1.0 km @ 1/2 CZ) is insufficient for this task, its much higher range resolution (~40 m) is exploited.[2] The basic idea behind the analysis is that when the bistatic measurement geometry is such that the receiving array's cross-range direction is skew to the ridge axis, characteristic nonlinearities in scarp structure, such as canyons (~100–200 m wide) and gullies (~50 m wide) previously documented with high-resolution supporting bathymetry,[2,3] become potentially resolvable by the towed-array system in range. The analysis of a full suite of such bistatic measurements, spanning ±90° about ridge-axis broadside, could lead to a detailed accounting of the scarp's nonlinear structure. Experimental uncertainties in the orientation of the towed-array, sound-speed structure and source–receiver navigation as well as statistical fluctuations in the scattered returns are difficult to account for *a priori* and can severely degrade the system's theoretical resolution. The value of the present analysis lies in its *experimental* assessment of a towed-array imaging system's resolving power.

The second main objective is to experimentally determine the inherent bi-azimuthal scattering distribution of the primary scatterers on the B' abyssal hill, namely two primary scarps that run along its major axis, when waterborne propagation paths are effectively horizontal at the abyssal hill, as they are in remote sensing applications. The hope is that the bi-azimuthal scattering distributions measured for

[a]Electronic mail: makris@mit.edu

Report Documentation Page

Form Approved
OMB No. 0704-0188

1. REPORT DATE	2. REPORT TYPE	3. DATES COVERED
NOV 1999		**00-00-1999 to 00-00-1999**

4. TITLE AND SUBTITLE	5a. CONTRACT NUMBER
The Bi-azimuthal Scattering Distribution of an Abyssal Hill	5b. GRANT NUMBER
	5c. PROGRAM ELEMENT NUMBER
6. AUTHOR(S)	5d. PROJECT NUMBER
	5e. TASK NUMBER
	5f. WORK UNIT NUMBER
7. PERFORMING ORGANIZATION NAME(S) AND ADDRESS(ES) **Massachusetts Institute of Technology,Cambridge,MA,02139**	8. PERFORMING ORGANIZATION REPORT NUMBER
9. SPONSORING/MONITORING AGENCY NAME(S) AND ADDRESS(ES)	10. SPONSOR/MONITOR'S ACRONYM(S)
	11. SPONSOR/MONITOR'S REPORT NUMBER(S)

12. DISTRIBUTION/AVAILABILITY STATEMENT
Approved for public release; distribution unlimited

13. SUPPLEMENTARY NOTES

14. ABSTRACT

15. SUBJECT TERMS

16. SECURITY CLASSIFICATION OF:			17. LIMITATION OF ABSTRACT	18. NUMBER OF PAGES	19a. NAME OF RESPONSIBLE PERSON
a. REPORT	b. ABSTRACT	c. THIS PAGE			
unclassified	**unclassified**	**unclassified**	**Same as Report (SAR)**	**22**	

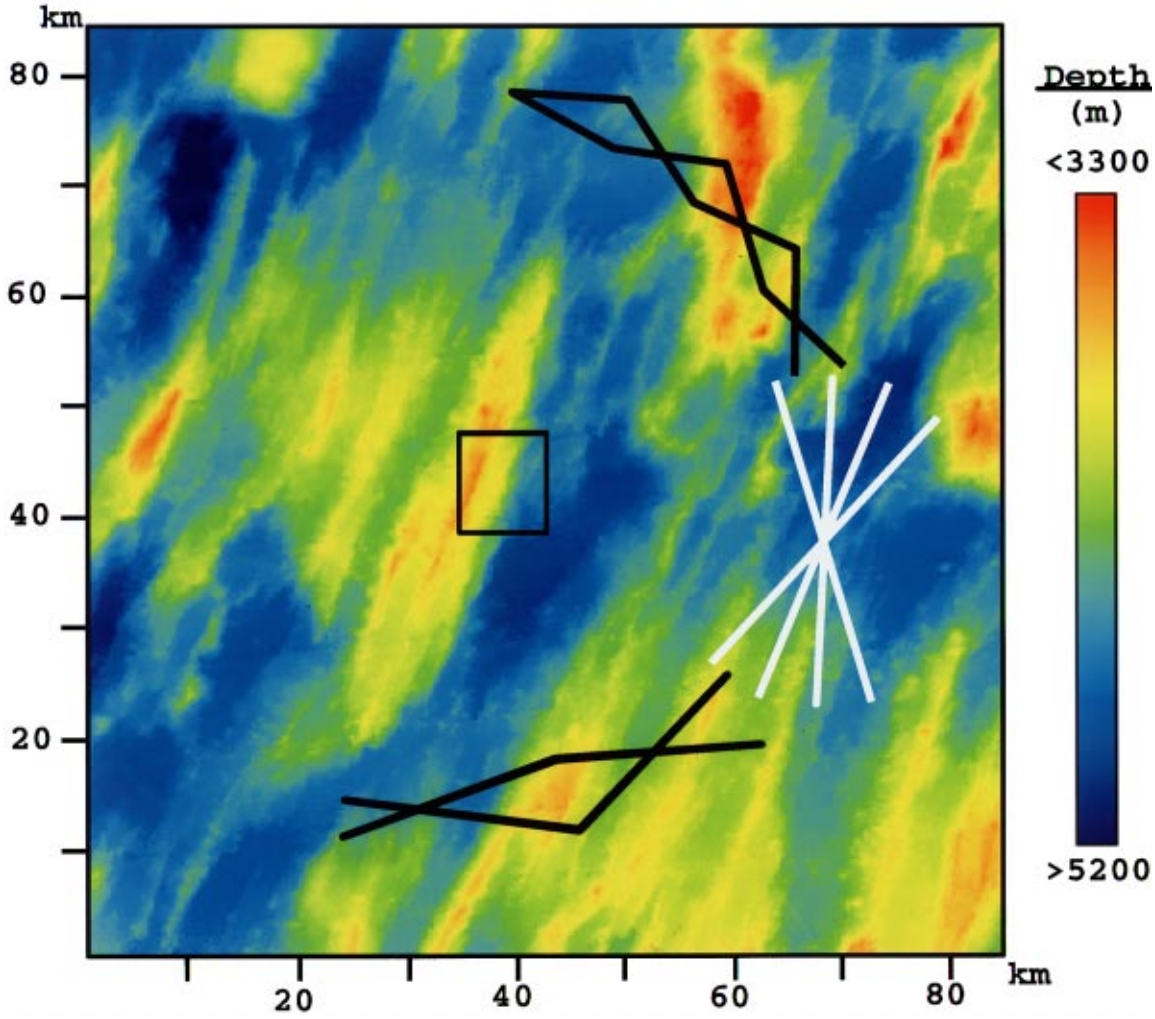

FIG. 1. The bistatic tow-ship tracks of the RV CORY CHOUEST (white lines) and RV ALLIANCE (black lines) during the B' experiment overlain on hydrosweep bathymetry (200-m sampling). The box indicates the region where high-resolution bathymetry (5-m sampling) is available. Conjugate depth with respect to the CORY source falls at 3800 m. Tracks for the entire $B'-C'$ experiment are shown in Ref. 2.

these may apply more generally to scarps found on abyssal hills throughout the MAR, many of which share the same highly lineated character. This type of knowledge about the scattering properties of abyssal hills is important because it enables one to (1) efficiently model bistatic scattering from abyssal hills, which often appears as clutter in active sonar systems operating in the deep ocean;[4] (2) ground-truth the output of seismo-acoustic scattering models with an empirical scattering function; and (3) classify bathymetric features according to their scattering properties so similar features may be identified in future towed-array surveys where there is no supporting bathymetric database.

To generalize the present bistatic scattering measurements, such effects as two-way transmission loss, the areal resolution of the measurement, and its foreshortening must be factored from them. In particular, high-resolution bathymetry, sampled at the scale of the acoustic wavelength, is used to determine surface orientation and foreshortening. The parabolic equation is used to compute two-way transmission, ray tracing to determine incident and scattered angles with respect to the seafloor surface, and a spatial convolution to account for the spatially varying areal resolution of the measurement system. Statistical fluctuations due to nonlinear speckle noise inherent in the measurements are reduced by stationary averaging and are stabilized by logarithmic transformation. Since all measurements of B' are at 1/2 CZ standoff, acoustic paths from the source and to the receiver are nearly horizontal when they intersect B'. This enables a relatively accurate calculation of the bi-azimuthal scattering distribution of the B' scarps which will be useful in the classification of similar scarps on mid-ocean abyssal hills by towed-array systems at $n+1/2$ CZ.

I. BISTATIC EXPERIMENTAL DESIGN, IMAGING RESOLUTION, AND THE GEOMORPHOLOGY OF THE B' ABYSSAL HILL

The geometry of the bistatic experimental survey of the B' abyssal hill is summarized here in Fig. 1, where the track design,[5,6] is overlain on hydrosweep bathymetry, sampled at 200-m intervals.[2,7] A more complete description of the $B'-C'$ corridor experiments, which comprised roughly 90% of MAE, can be found in Refs. 2, 5, and 6. The 8×9-km^2 box at the center of B' shows the region where high-

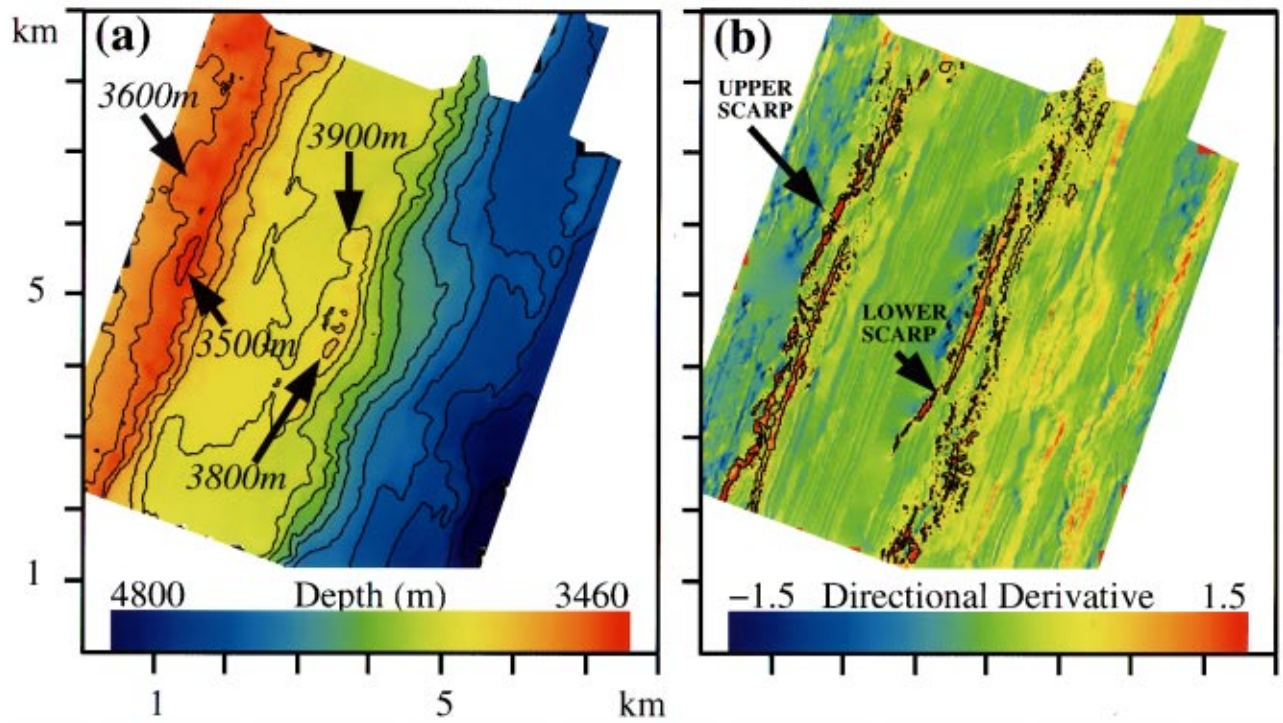

FIG. 2. (a) High-resolution bathymetry (5-m sampling) on the east-central face of B' as located in Fig. 1. Depth contours are at 100-m intervals. (b) The component of seafloor elevation gradient, or the directional derivative (DD), normal to the B' axis, computed from high-resolution bathymetry as in Fig. 22 of Ref. 2. Many steep cliffs (>60° slope) and smaller terraces (~45° slope) appear on both the upper and lower scarps that cannot be resolved by the hydrosweep bathymetry. Contours segment the upper and lower scarps as regions within which the DD exceeds 1/2. These same contours are used to identify the scarps throughout this paper.

resolution bathymetry, sampled at 5-m intervals, was collected in support of MAE.[2,3] The research vessel (RV) CORY CHOUEST traced the central star while the RV ALLIANCE followed the wings to the north and south. Each RV towed a horizontal receiving array with axis roughly coincident with the ship's straight-line course. To maximize cross-range resolution of B' and to minimize noise contamination from the other RV, the highest resolution beams at array broadside are directed towards the center of B', where high-resolution bathymetry is available, while the lowest resolution beams at array endfire are directed towards the other RV.[2,4,6] Only transmissions from the CORY CHOUEST source array are considered in this paper because of its significantly higher strength, 229 dB *re* 1 mPa @ 1 m, and directionality compared to that of the ALLIANCE.[2,8] The CORY's source array is steered to broadside for all transmissions studied in this paper.

Linear frequency modulated (LFM) waveforms of $\tau = 5$ s duration in the frequency band 200–255 Hz are exclusively analyzed here because they offer the highest available range resolution, which is given by $\Delta r = c/(2B) \sim 14$ m, where $c \sim 1510$ m/s is the mean sound speed and B is the bandwidth.[2] To reduce their standard deviation after pulse compression, instantaneous intensity measurements are averaged over time period $T = 0.0625$ s for CORY receptions and $T = 0.0533$ s for ALLIANCE receptions. This averaging leads to an effective range resolution of $\Delta r = cT/2 = 47$ m for the CORY and $\Delta r = 40$ m for the ALLIANCE.

With the assumption that the specific bathymetric features resolved by the towed-array system behave as Rayleigh targets,[9,10] due to their structural complexity with respect to the wavelength scale, the degrees-of-freedom $N \sim TB$ becomes roughly 3.4 for CORY and 2.9 for ALLIANCE LMF receptions. The further assumption of independence and stationarity among the roughly 3 range cells averaged leads to a standard deviation of 2.5 dB and a bias of 0.6 dB in the intensity level at any pixel of a towed-array image.[2,10] If, on the other hand, a particular range cell dominates the average, or if the range cells are correlated, μ may be as small as unity, which leads to a standard deviation of roughly 5.6 dB and a bias of 2.5 dB.[2,10]

The geomorphology of the B' abyssal hill is displayed in Fig. 2. Gross features are evident in the high-resolution bathymetry of Fig. 2(a). The central crest of B', for example, rises roughly 1400 m from the western segment valley floor at roughly 4900 m to nearly 400 m above the 3800-m conjugate depth[2] of the CORY source. Minute details of the high-resolution bathymetry are best cast in terms of the component of seafloor elevation gradient, or directional derivative, normal to the B' axis, shown in Fig. 2(b). This reveals two steep scarps separated by an extended plateau just below 3800 m. Both scarps run along the B' axis 21° from true North, and are characterized by steep unsedimented cliff faces that rise upwards for typically 100 m with characteristic slopes of 50°–90°. The scarps are segmented by a contour within which the directional derivative exceeds 1/2, corresponding to slope angles greater than ~26.6°. The contours, shown in Fig. 2(b), are used throughout the paper to designate the locations of the upper and lower scarps.

The bistatic locations of the two research vessels during

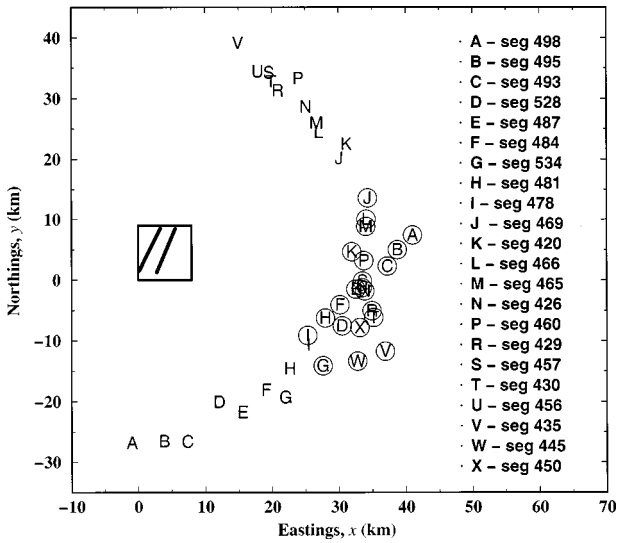

FIG. 3. The bistatic locations of the two research vessels during the LFM transmissions analyzed in this paper are given in eastings, *x*, and northings, *y*. These locations are distributed in a semicircle about the high-resolution region shown by the central box within which two diagonal lines indicate the upper and lower scarps. Circled letters indicate the location of the CORY while the same letters indicate the location of the ALLIANCE for the 20 bistatic segments given in the legend. Segments S430, S466, S481, and S495 are excluded from the monostatic analysis due to colocation with some of the other monostatic segments shown. Since ALLIANCE was at the apex of the northern wing and in the shadow of B' during S445 and S450, they are used as the only purely monostatic transmissions in this analysis, which then has a total of 18 monostatic segments.

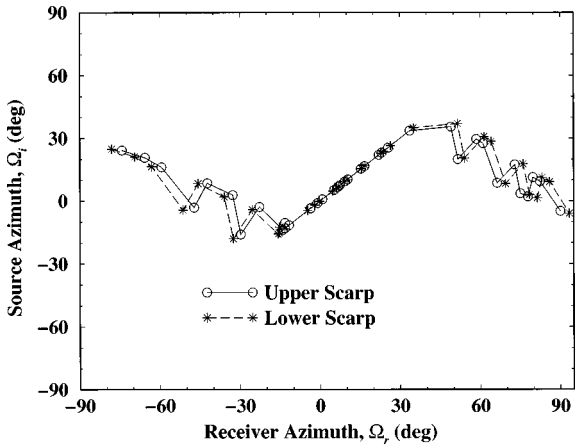

FIG. 4. The portion of bi-azimuthal space spanned by the source–receiver pairs. Azimuth is measured counterclockwise from a vector that originates from the center of the given scarp in the high-resolution region and points normal to its axis in a southeasterly direction. Source azimuths are denoted by Ω_i and receiver azimuths by Ω_r. The curves for the upper and lower scarps are nearly identical because their separation is small compared to the range to the respective RV. The portion of nonmonostatic space spanned is double that shown by acoustic reciprocity between source and receiver locations.

the LFM transmissions analyzed in this paper are given in eastings and northings in Fig. 3. These locations are distributed in a semicircle with bisecting diameter oriented along the B' axis and centered in the high-resolution region. A letter of the alphabet designates each transmission. Circled letters indicate the monostatic location of the CORY while unboxed letters indicate the bistatic location of the ALLIANCE for a given transmission. A *segment number* specifies each transmission, following the vernacular of the MAE.[1,2]

The portion of bi-azimuthal space spanned by the source–receiver pairs is shown in Fig. 4. Azimuth is measured counterclockwise from a vector that originates from the center of the given scarp in the high-resolution region and points normal to its axis in a southeasterly direction. The source azimuths Ω_i then fall within $|\Omega_i|<30°$, while the receiver azimuths Ω_r span the full 180° range. This bistatic geometry is appropriate because (1) the east-central face of B' is uniformly insonified with negligible shadowing, and (2) the receivers are never completely shadowed.

Expressions for the half-power or 3-dB beamwidth $\beta(\theta)$ of a narrow-band line array, steered to an angle θ from endfire, are given in Eqs. (1) and (2) of Ref. 11 as a function of aperture length and frequency. These expressions also approximate the azimuthal resolution of the MAE arrays for LFM reception when evaluated at the LFM center frequency of 227.5 Hz. Best resolution lies at broadside and is ~1.6° for the $L=318$ m receiving array of the CORY and ~2.0° for the $L=254$ m receiving array of the ALLIANCE. Cross-range resolution, defined as $r\beta(\theta)$ for a monostatic measurement at range r from the scattering patch, is then 0.9 km for the CORY and 1.1 km for the ALLIANCE at 1/2 CZ where $r=33.3$ km.

At 1/2 CZ, neither array has sufficient aperture to azimuthally resolve characteristic nonlinearities in scarp structure, such as canyons (~100–200 m wide) and gullies (~50 m wide) previously documented with high-resolution supporting bathymetry.[2,3] This is evident upon inspection of Fig. 5(a), where the resolution footprint of the towed-array system, a roughly 50 m by 1 km annular sector at 1/2 CZ, is superimposed on a bathymetric image of the B' upper scarp. These same features become potentially resolvable by the towed-array system in range when cross-range is skew to the ridge axis, as shown in Fig. 5(b), with the relatively safe assumption that the scarp, and not the plateaus above and below, cause the predominant reverberation. Analysis of a full suite of such bistatic measurements, spanning $|\Omega_r|<90°$, could provide a detailed accounting of the scarp's nonlinear structure, given sufficient charting accuracy and statistical stability of the measured reverberation.

The normalized autocorrelation function of upper scarp elevation, in Fig. 6, quantitatively reveals along and across-scarp correlation scales (*e*-folding lengths) of 150 and 50-m, respectively, consistent with a visual assessment of typical canyon and gully dimensions. The resolution footprint of the towed-array system integrates or blurs together scattered returns from roughly five major canyons when its cross-range range axis parallels the scarp's, as is characteristic of the monostatic measurements. This leads to a broad distribution of incident angles from a given source, or scattered angles to a given receiver, over the resolution footprint. This is shown in Fig. 7(a) for S435 where vertical refraction is taken into account via raytrace. Conversely, the resolution footprint typically blurs together scattered returns from the outer wall of a single canyon with those from plateaus above and below when its cross-range axis is skew to the scarp axis, as is characteristic of bistatic measurements with large $|\Omega_r|$. This

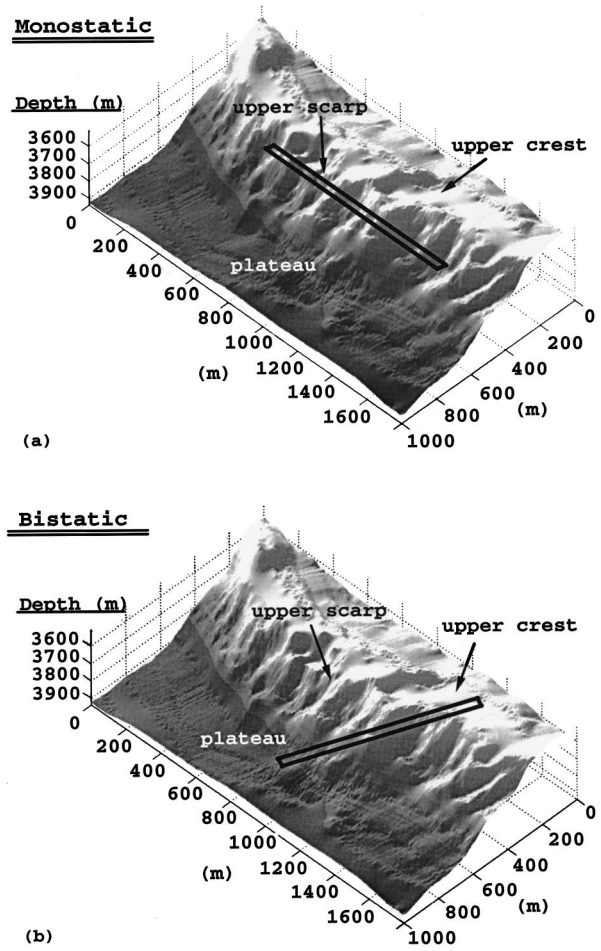

FIG. 5. Shaded relief of a portion of the B' upper scarp imaged with high-resolution bathymetry with the roughly 50-m by 1-km resolution footprint of the towed-array system overlain. (a) Monostatic geometry for S435. (b) Bistatic geometry for S435. In (a), the resolution footprint blurs together many characteristic nonlinearities in scarp structure, such as canyons and gullies. These features become potentially resolvable in range, as in (b), for some bistatic geometries of the present experiment.

also leads to a broad distribution of incident angles or scattered angles over the resolution footprint, as shown in Fig. 7(b) and (c) for the same segment.

Since the surfaces resolved by the towed-array system on the B' scarps are not even approximately planar, there is no unique surface normal to characterize the bathymetry within the resolution footprint. Consequently, there is no unique incident or scattered angle. The *traditional surface scattering strength*, which depends upon the directions of incident and scattered waves defined relative to the local surface normal and *includes purely local foreshortening effects*, must then be reanalyzed to accommodate the reality of the present experiment, as will be discussed in later sections.

II. BISTATIC IMAGING OF THE B' ABYSSAL HILL FROM 1/2 CZ

A. Wide-area bistatic images

While a number of *monostatic*, reverberation charts of the B' abyssal hill have been presented and analyzed,[2,12–14] only two *bistatic* charts of B' have been previously studied in the literature.[2] These are for the 200–255-Hz LFMs of

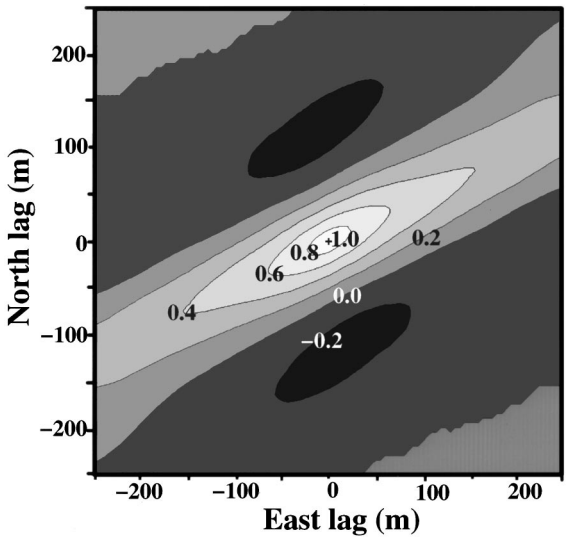

FIG. 6. The normalized 2-D autocorrelation of upper scarp elevation as a function of east and north spatial lag. The along-scarp and across-scarp *e*-folding lengths of ~150 and ~50 m, respectively, quantify the scale of typical nonlinearities along and across the scarp.

S478 and S487. Analysis of S478 is particularly significant because it characterizes all measurements for which the bistatic separation between the CORY and ALLIANCE is small relative to the range to B'. In these cases, bistatic and monostatic charts are similar with cross-range falling parallel to the B' axis. Prominent reverberation is then unambiguously charted to the steep escarpments, as demonstrated in Ref. 2. Monostatic and bistatic reverberation charts of the same transmission show great differences, however, when the bistatic separation is large. This is well illustrated here for S435 and S528, which are respectively at the northern extreme and midway to the southern extreme of the ALLIANCE

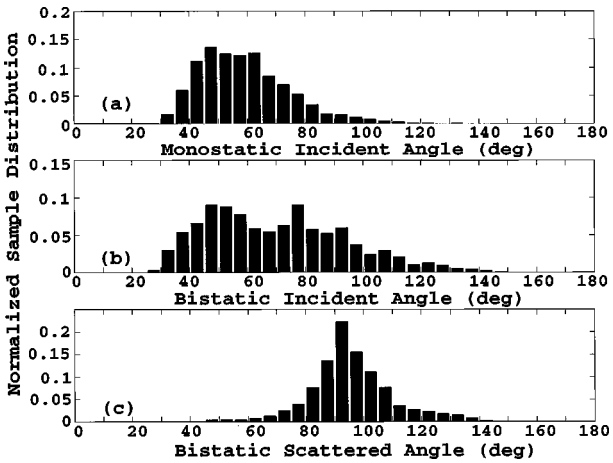

FIG. 7. The distribution of incident and scattered angles within the resolution footprints shown in Fig. 5 for S435. The incident angle is the inverse cosine of the inner product between the local surface normal and the vector pointing along the acoustic path to the source. The scattered angle is the inverse cosine of the inner product between the local surface normal and the vector pointing along the acoustic path to the receiver. Refraction is included. Angles greater than 90° indicate shadowing. (a) Monostatic case where incident and scattered angles are identical and axis of resolution footprint is along scarp axis. Bistatic case for (b) incident angles and (c) scattered angles, where axis of resolution footprint is skew to scarp axis.

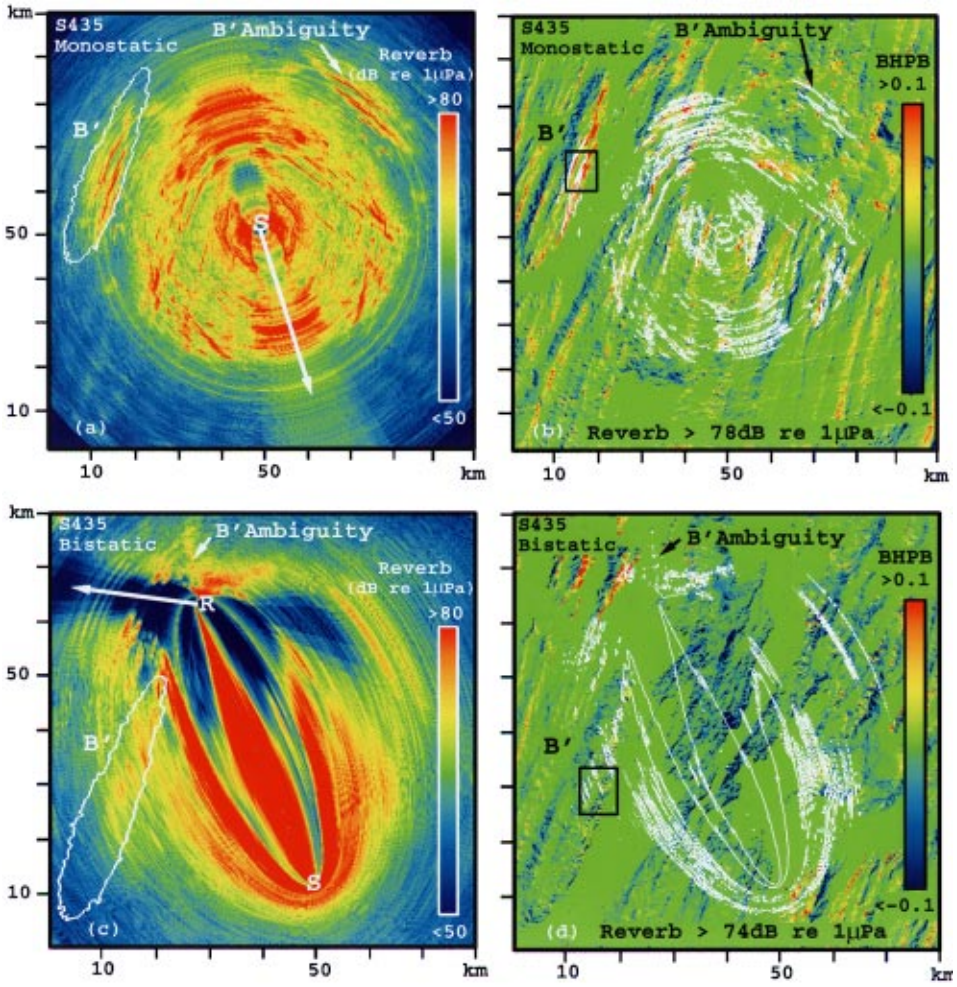

FIG. 8. Wide-area charts of monostatic and bistatic reverberation measured for the 200–255-Hz LFM S435, where ALLIANCE is near the apex of the northern wing. (a) Monostatic reverberation chart showing symmetry about the array axis for CORY heading 163°. (b) Contours of high-level backscatter, overlain on the bistatic horizontal projection of bathymetry (BHPB), coregister with major scarps on B' that have large areas projected towards the source–receiver. The false backscatter image of B' does not coregister with the BHPB. (c) Bistatic reverberation chart shows asymmetry about the array axis because this axis forms an oblique angle with the major axis of the bistatic ellipse. The ALLIANCE heading is 277°. (d) Contours of high-level backscatter, overlain on the BHPB, coregister with major scarps on B' that have large areas projected along the acoustic path from source to scatterer to receiver. Unlike the monostatic case, the cross-range axis of the resolution footprint forms an oblique angle with the scarp axis so that prominent returns are speckled across the scarp. The false backscatter image of B' does not coregister with the BHPB and exhibits severe spatial contraction. Source and receiver locations are indicated in (a) and (c). The product of a negative HPBR and a negative HBPS is always plotted as a negative HPBR to distinguish shadowed regions.

tracks. Specifically, $\Omega_i \sim -5°$ and $\Omega_r \sim 90°$ for S435 and $\Omega_i \sim -5°$ and $\Omega_r \sim -50°$ for S528, with respect to both upper and lower scarp reference centers.

To gain a broader perspective, consider first the wide-area charts of monostatic reverberation, in Figs. 8–10(a). These each have a character very similar to that found for short continuous wave (cw) transmissions in Figs. 8 and 9 of Ref. 2. When overlain on the bistatic horizontal projection of bathymetry (BHPB), prominent reverberation coregisters precisely with steep escarpments along the B' axis, as illustrated in Figs. 8–10(b). The bistatic horizontal projection of bathymetry is the product of the horizontal projection of bathymetry toward the source (HPBS) and the horizontal projection of bathymetry toward the receiver (HPBR). The former is inner product of the local seafloor normal and a unit vector pointing to the horizontal position of the source, while the latter is the inner product of the local seafloor normal and a unit vector pointing to the horizontal position of the receiver. To distinguish shadowed regions, the product of a negative HPBR and a negative HBPS is always plotted as a negative HPBR. In later sections, a far more precise computation of surface projection factors, accounting for refracted ray paths to and from the seafloor, is employed to analyze reverberation over the region of high-resolution bathymetry.

In the general limiting case of range-independent propagation and a flat bottom, range ambiguity of the bistatic towed-array system falls on elliptic arcs about foci coinciding with the source and receiver positions. The arcs are defined by conserving the two-way travel distance from source to scatterer to receiver as the sum of the radii. The arc length at 1/2 CZ, over the broadside resolution of the CORY or ALLIANCE receiving array, remains well approximated by the monostatic cross-range resolution $r\beta(\theta)$ for the entire suite of bistatic measurements taken at B', as shown in Appendix A. Here, r is range from the receiving array to the scattering site. For what we refer to here as ''monostatic'' measurements, the CORY's source and receiver arrays are not coincident but are in such close proximity (~1.12-km separation) that range ambiguity lies on nearly circular arcs at 1/2 CZ. When the bistatic separation between the CORY and ALLIANCE is not small compared to r, however, the arcs are far from circular. This accounts for some characteristic differences between monostatic and bistatic charts of the same transmission.

The right–left ambiguity of the receiving line array is also expressed differently in monostatic and bistatic charts. Prominent features are ambiguously charted in an almost symmetrical fashion about the receiving array's axis in monostatic geometries.[11,2] Only the incorporation of known bathymetry in the charting procedure leads to local breaks in symmetry.[2,14] Such extreme symmetry, however, is only

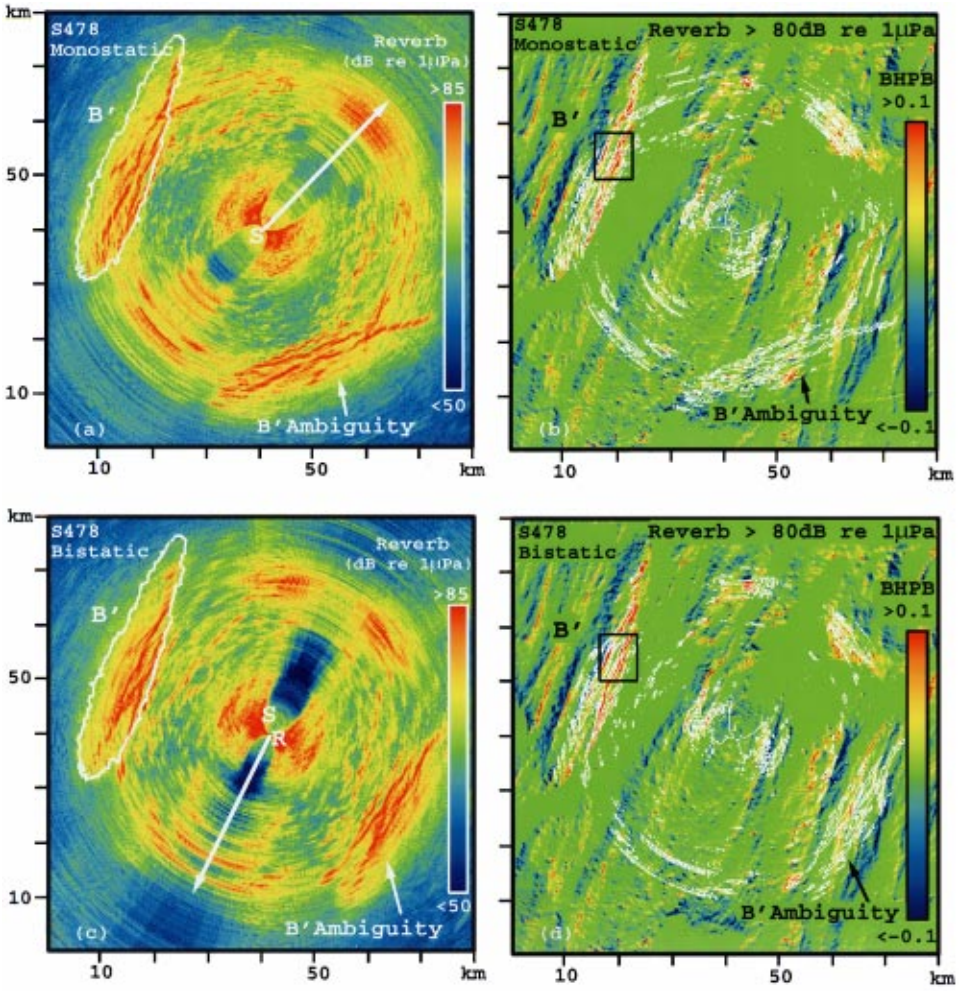

FIG. 9. Wide-area charts of monostatic and bistatic reverberation measured for the 200–255-Hz LFM S478. ALLIANCE and CORY are in close proximity. (a) Monostatic reverberation chart showing symmetry about the array axis for CORY heading 45°. (b) Contours of high-level backscatter, overlain on the BHPB, coregister with major scarps on B' that have large areas projected towards the source–receiver. (c) Bistatic reverberation chart shows symmetry about the array axis due to the close proximity of the CORY and ALLIANCE. The ALLIANCE heading is 207°. (d) Contours of high-level backscatter, overlain on the BHPB, coregister with major scarps on B' that have large areas projected along the acoustic path from source to scatterer to receiver.

available in bistatic scenarios when the receiving array axis parallels the line joining the source and receiver. This line defines the major axis of the bistatic ellipse. Otherwise, some distortion occurs. In the case of segment 435, the receiving array is at an oblique angle to the major axis of the bistatic ellipse. Prominent reverberation from the central scarps of B' correctly register at roughly 1/2 CZ (~33.3 km) from the receiving array. The corresponding ambiguous returns are mirrored about the array axis, and span the same annular sector as the true returns, but fall at a much shorter range to preserve the travel time. As a result, they are condensed to a much smaller spatial area than that spanned by the true returns. The converse is also true. True returns from this small area, where the right–left ambiguity of the receiving array intersects the elliptical range ambiguity of the bistatic system, may be falsely charted to a more extensive region on B'. The geometry of this type of ambiguity is given in Fig. A1. After a careful analysis of the registration between bathymetric directional derivatives and prominent reverberation, we find that the experimental design[5] was successful in exploiting the natural geomorphology of the region to avoid contamination from line-array ambiguity at B'.

Prominent bistatic returns are overlain on the bistatic horizontal projection of bathymetry (BHPB) in Figs. 8–10(d). In the limit of horizontal propagation to and from the bottom, which is a reasonable approximation for waterborne paths at $n+1/2$ CZ, the BHPB becomes a projection factor directly proportional to the incoherent intensity of the scattered field from an infinitesimal area of the seafloor, and so is useful for comparison with wide-area reverberation.

For large bistatic separations, as in S435 and S528, characteristic nonlinearities in scarp structure, such as canyons and gullies, lead to a speckled pattern of strong projections in the path connecting source, scatterer, and receiver. Over the same region, prominent bistatic reverberation displays analogous behavior as a speckled pattern of concentric arcs that obliquely cross the scarp axes. This phenomenon was previously observed in monostatic reverberation charts when the radial propagation path was parallel to or formed a shallow angle with the axis of a major bottom-limited ridge.[2] The effect is partially due to (1) anomalous surface projections, and (2) statistical fluctuations from random interference, as will be shown in the next sections.

B. High-resolution images of the east-central face of B'

The bending of acoustic paths from the source, to the scattering patch and back to the receiver, caused by naturally occurring depth-dependent variations in the ocean's refractive index, described in Ref. 2, must be taken into account for the charting accuracy of long-range echoes to be compa-

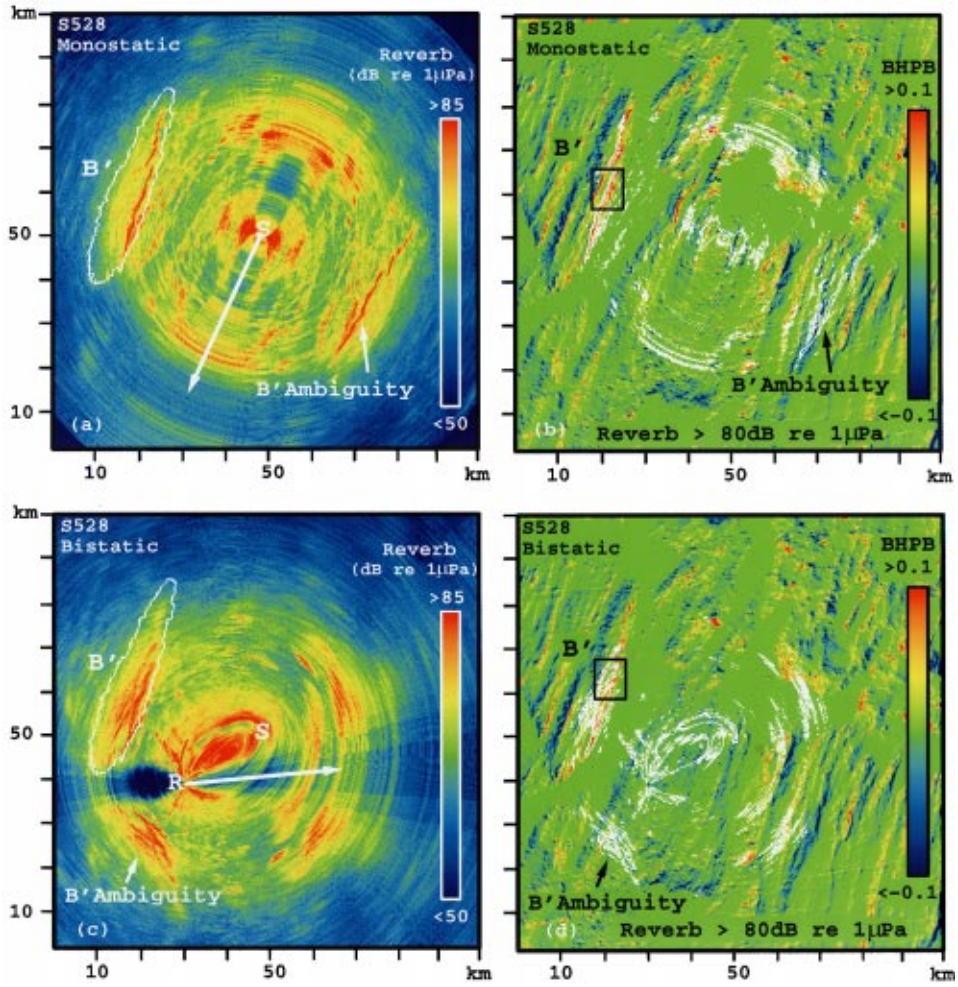

FIG. 10. Wide-area charts of monostatic and bistatic reverberation measured for the 200–255-Hz LFM S528. Alliance is midway along the southern wing. (a) Monostatic reverberation chart showing symmetry about the array axis for CORY heading 206°. (b) Contours of high-level backscatter, overlain on the BHPB, coregister with major scarps on B' that have large areas projected towards the source–receiver. The false backscatter image of B' does not coregister with the BHPB. (c) Bistatic reverberation chart shows asymmetry about the array axis due to the oblique angle it forms with the major axis of the bistatic ellipse. The ALLIANCE heading is 87°. (d) Contours of high-level backscatter, overlain on the BHPB, coregister with major scarps on B' that have large areas projected along the acoustic path from source to scatterer to receiver. The false backscatter image of B' does not coregister with the BHPB and exhibits severe spatial contraction.

rable to the 5-m sample interval of the high-resolution bathymetry shown in Fig. 2. A sophisticated, range-dependent ray-based propagation model known as RASP,[15] that includes the effects of multiple interactions between surface and bottom boundaries, was used to chart reverberation out to multiple CZ ranges in Ref. 2. A number of other methods have been developed and employed by other SRP researchers.[13,14,16]

For the purpose of the present analysis, where only waterborne insonification of the high-resolution area is considered, a somewhat simpler but more efficient raytrace model is used to obtain the two-way travel times. Rays are traced in a range-depth plane from a point source, located at the center of the respective source or receiving array, through a refractive ocean half-space with a pressure-release surface but no bottom boundary. Surface-reflected paths are accounted for, but the much slower and more attenuated bottom-reflected paths are neglected. Range-depth maps of minimum travel time are then generated. A range-depth map is then swept through the high resolution bathymetry of B' to determine minimum travel time to or from the bottom. This procedure is repeated for all source and receiver locations to obtain respective travel time maps in the horizontal plane over the high-resolution region. These maps are then used to chart the output of the beamformed and matched filtered reverberation data to the high-resolution region by the same bistatic mapping algorithm employed in Refs. 2, 11, and 12. Navigation data from the Global Positioning System (GPS)[17] of each RV are precisely converted to universal transverse Mercator (UTM)[18] coordinates, for long-range reverberation charting, by the United States Geological Survey (USGS) geodetic reference system[19] that is accurate to within roughly 1 m.

The error in computing travel time to the high-resolution region by slant-range, rather than raytrace, is illustrated in Fig. 11. Since the one-way errors shown are typically much greater than the roughly 0.003 s it takes to cross a 5-m sample interval of high-resolution bathymetry at the mean sound speed, the slant-range approach to charting reverberation is unacceptable.

High-resolution images of charted reverberation are illustrated in Figs. 12–14 for segments 435, 478 and 528, with contours overlain to specify locations of the upper and lower scarps. Both scarps tend to appear prominently and faithfully imaged in the monostatic charts, as in S478 and S435. This fidelity is possible because the cross-range axis of the resolution footprint lies along the scarp axes. In some segments, such as S528, however, the entire upper scarp vanishes amidst low-level background reverberation. This happens when the upper scarp falls in the shadow zone of the main beam's refractive path, due to its proximity to the source array's conjugate depth.[2] The lower scarp appears prominently in all monostatic charts because it lies below the

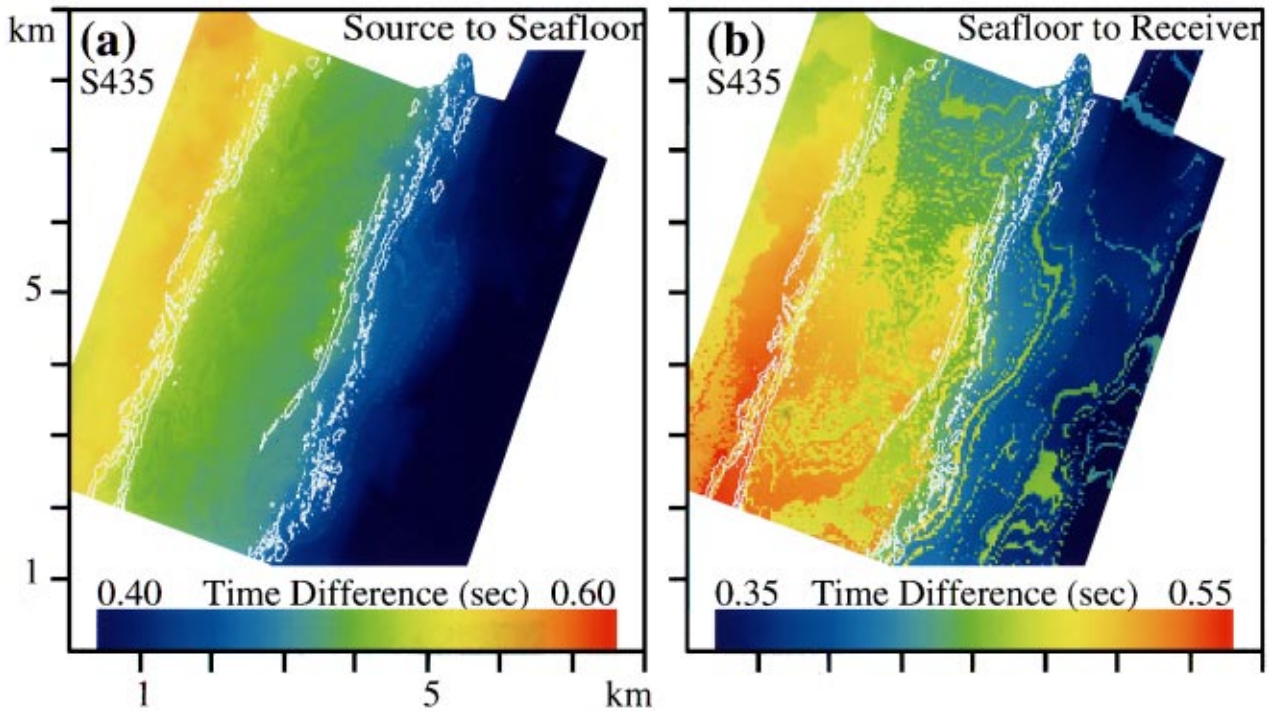

FIG. 11. (a) Slant-range travel time, using mean sound speed along the slant path, minus raytrace travel time from CORY source to seafloor for S435 using high-resolution bathymetry. (b) Same as (a) except from seafloor to ALLIANCE receiver for S435. These one-way errors are typically much greater than the 0.003-s travel time it takes to cross a 5-m sample interval of high-resolution bathymetry.

shadow zone, displayed in Fig. 15(a), and generally receives main-beam insonification.

The consistent coregistration between the locations of the strongest monostatic returns and the locations of the scarps carries much statistical weight. The upper 5% of reverberation within the high-resolution area is selected for each segment to demonstrate this. The frequency of overlap of these selected regions, over all 18 monostatic segments, is plotted in Fig. 16(a) together with overlays of the upper and lower scarps. This figure shows that the regions that most frequently return the strongest backscatter coincide with some of the steepest portions of the upper and lower scarps. The figure also shows that the frequency of strong backscatter rapidly decreases as the distance from the scarp increases in the cross-scarp direction. It is extremely unlikely, for example, to find even a single strong return charted to points lying at ranges beyond roughly 1.0 km of either scarp.

The bistatic charts for S435 and S528 are significantly different from the corresponding monostatic charts, as noted in the wide-area analysis of the previous section. The difference arises because the system's cross-range resolution is at an oblique angle to the scarp axes in the bistatic case, whereas it parallels it in the monostatic case. Prominent bistatic returns lie along nearly elliptical arcs centered across the scarp axes. This is seen in Figs. 12–14, which are typical of many of the bistatic segments studied. The strongest returns appear in a speckled fashion along the scarps axis. In extreme cases where cross-range is nearly normal to the scarps axes, as in S435, the towed-array system is sometimes unable to distinguish the upper from the lower scarp. This effect is apparently due to the relatively close proximity of the two scarps, roughly 2 km separation or twice the cross-range resolution of the receiver, and occasionally leads to strong returns continuously charted across both scarps in elliptic arcs centered through the plateau. This may lead one to the presumably *false* conclusion that the plateau contains geomorphological anomalies that may yield strong returns.

The spatial frequency distribution of the most prominent bistatic returns is shown in Fig. 16(c). As in the monostatic case, the upper 5% of reverberation over the high-resolution area is selected for each segment. The overlap frequency of these selected regions, across all 20 bistatic segments, is plotted together with overlays of the upper and lower scarps. While the global maxima appears on the steepest portion of the upper scarp, and local maxima often register with both the upper and lower scarps, the largest number of local maxima appear in the region between the scarps. Frequency tends to decrease as range increases from the region between and including both scarps. Single-frequency returns, however, remain densely spread with relative uniformity from the upper crest to the lower scarp, and only begin to disappear as the trench below the lower scarp is approached. While some cross-hatching of overlain returns is to be expected just above and below the upper and lower scarps, due to a combination of ridge morphology, track geometry, and cross-range blurring, the significantly higher concentration of high frequencies between the upper and lower scarps rules this combined effect out as the sole cause of off-scarp charting of prominent reverberation, as is shown in the next section. An explanation for the measured frequency distribution follows in Sec. II D.

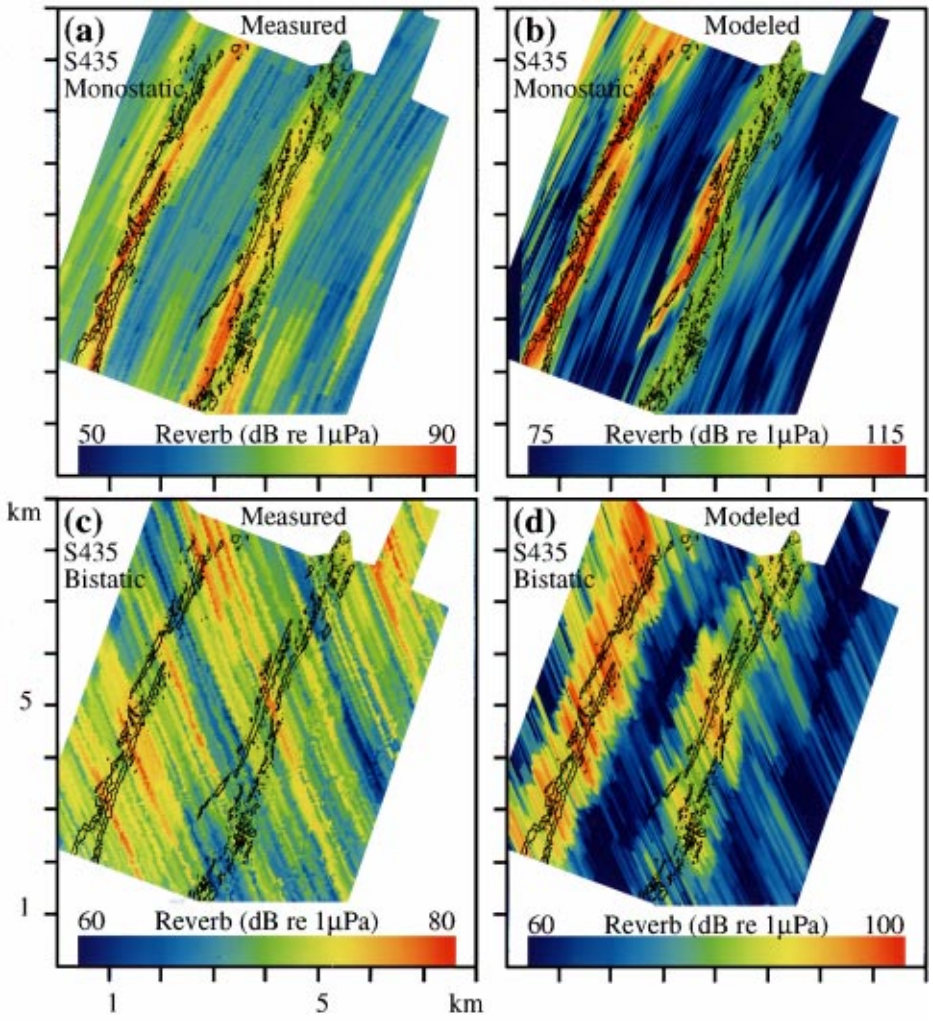

FIG. 12. High-resolution charts of monostatic and bistatic measured and modeled reverberation for S435 over the region shown in Fig. 2 with upper and lower scarp contours overlain. (a) Measured monostatic reverberation. (b) Modeled monostatic reverberation. (c) Measured bistatic reverberation. (d) Modeled bistatic reverberation.

C. Modeling high-resolution reverberation and estimating the scattering distribution

From an infinitesimal planar surface patch of area dA, in the far field of a source and receiver, the scattered intensity at the receiver can be written as

$$dI = f(\theta_i, \phi_i; \theta_r, \phi_r) w l_i l_r \cos\theta_i \cos\theta_r dA, \tag{1}$$

according to the basic principles of radiometry. Here, θ and ϕ denote polar and azimuth angles with respect to the local surface normal,[20] with incident and scattered angles identified by the subscripts i and r. The projected area of the surface patch in the direction of the scattered wave leaving the surface patch is $\cos\theta_r dA$. The other factors include the source power w, transmission coefficients l_i and l_r in inverse-square meters from the source to the surface patch and from the surface patch to the receiver, and the bidirectional scattering distribution function (BSDF) of the surface f,[20–22] which is a dimensionless parameter describing surface-scattering properties that are invariant in expected value to changes in transmission and projected area. It is noteworthy that $f\cos\theta_i\cos\theta_r$ is simply the antilog of the standard scattering strength of ocean acoustics[23] $S = 10\log(f\cos\theta_i\cos\theta_r)$, where f is essentially the quantity describing bidirectional surface ''reflectance'' properties that has become standard in radiometry after its introduction by the National Bureau of Standards in 1977.[21] A perfectly Lambertian surface, for example, has $f = 1/\pi$, whereas a perfectly specular surface has $f = \delta(\theta_i - \theta_r)\delta(\phi_i - \phi_r + \pi)/(\sin\theta_i \cos\theta_i)$. The latter singularity is necessary to escape the implicitly incoherent nature of a summation over dA in Eq. (1). When f is an angle-independent constant, it is related to the surface albedo[24] α by $f = \alpha/\pi$ and can be interpreted as becoming the constant μ associated with Mackenzie's formulation of seafloor scattering strength.[23]

It is practical to recast Eq. (1) in decibels, by dividing through by appropriate reference units and taking 10 log of both sides. This homomorphic transformation stabilizes the variance for optimal pattern recognition[10,25] and compresses the dynamic range. The result is

$$R_{dA} = F(\theta_i, \phi_i; \theta_r, \phi_r) + W - \mathrm{TL}_i - \mathrm{TL}_r + C_i + C_r + 10\log(dA/A_{\mathrm{ref}}), \tag{2}$$

where the reverberation level on the left in dB *re* 1 μPa is balanced by the scattering distribution's strength F, the source strength W in dB *re* 1 μPa @ 1 m, the transmission loss from the source to scattering patch TL_i, and from the scattering patch to the receiver TL_r, in dB *re* 1 m, the pro-

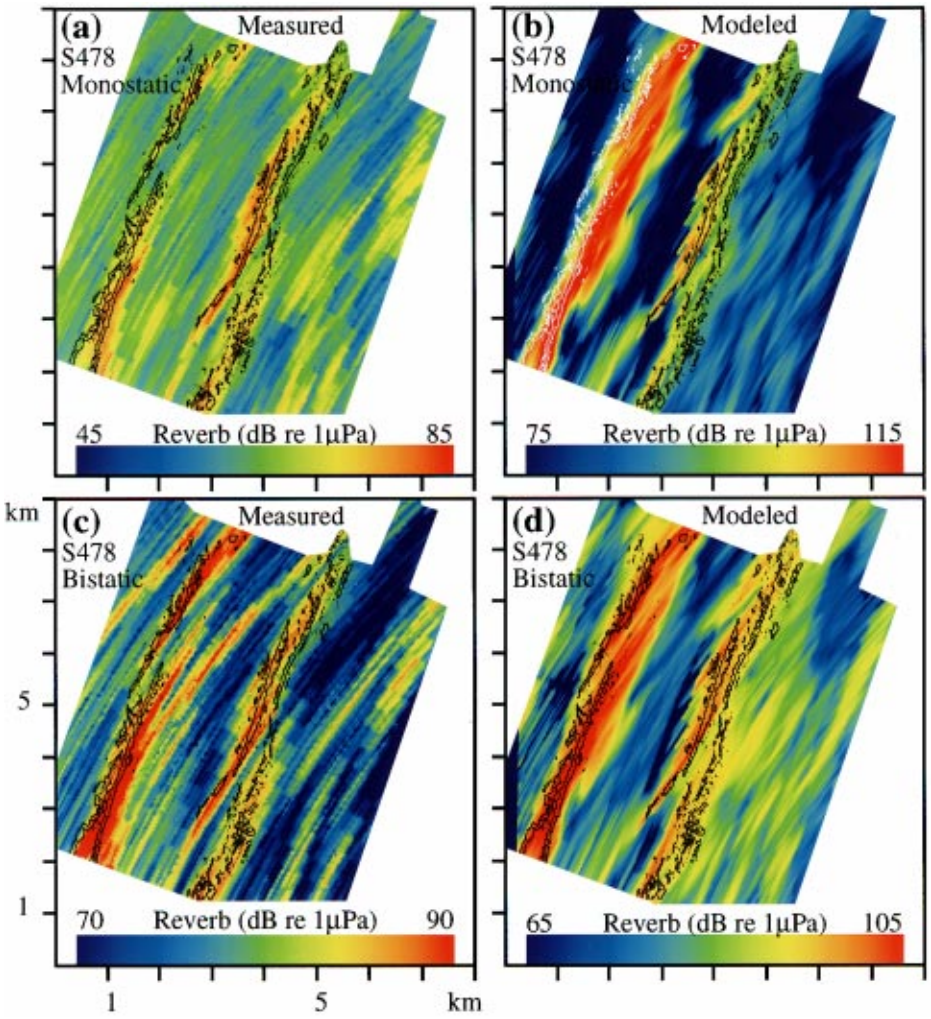

FIG. 13. High-resolution charts of monostatic and bistatic measured and modeled reverberation for S478 over the region shown in Fig. 2 with upper and lower scarp contours overlain. (a) Measured monostatic reverberation. (b) Modeled monostatic reverberation. (c) Measured bistatic reverberation. (d) Modeled bistatic reverberation.

jection terms $C_i = 10\log(\cos\theta_i)$, $C_r = 10\log(\cos\theta_r)$, and the area term, in dB *re* 1 m. With Cartesian coordinates for east and north specified by x and y, the differential area becomes $dA = dx\,dy$. In practice, the elements dx, dy represent the 5-m bathymetric sample interval of the high-resolution region of B', over which the seafloor can presumably be approximated as planar.

The strength of the bidirectional scattering distribution F then is *independent of the local seafloor foreshortening as seen from the perspectives of the source and receiver*, whereas the scattering strength S is not, so F is preferred over S as the parameter to empirically describe the inherent scattering properties of the MAR seafloor since there is no unique surface normal to characterize bathymetry within our system's resolution footprint.

To model reverberation, each of the spatially varying terms of Eq. (2), which excludes W and $10\log(dA/A_{\text{ref}})$, is charted in an x,y grid over the high-resolution region.

To compute the projection terms, range-depth maps of the propagation direction of minimum-travel-time rays spreading outward from a point source below a pressure-release surface are computed for a bottomless ocean, given the watercolumn sound-speed profile shown in Fig. 1 of Ref. 2. The point source is located (1) at the 181-m depth of the center of the CORY source array, for rays traveling to the virtual scattering surface, (2) at the 460-m depth of the ALLIANCE receiving array, by reciprocity, for rays traveling from the virtual scattering surface to the ALLIANCE receiver, and (3) at the 170-m depth of the CORY receiving array for rays traveling from the virtual scattering surface to the CORY receiver. The high-resolution bathymetry is then swept through the range-depth map to determine the incident and scattered angles at the bottom. The inner product of these angles with the local surface normal yields the cosine factors of Eq. (1), and log transformation yields the bathymetric projection terms of Eq. (2) that relate linearly to reverberation level.

Charts of transmission loss are computed in a similar fashion. Range-depth maps of the monochromatic field produced by a 10-element source array, computed using the parabolic equation,[26] are integrated across the 200–255-Hz frequency band of the LFM *incoherently*, to be consistent with actual rough surface scattering. The resulting incoherent broadband transmission loss, shown in Fig. 15(a), exhibits substantial structure with a well-defined main beam, the remnants of frequency-averaged Lloyd mirror interfering beams, and sidelobes. High-resolution bathymetry is then swept through this map to chart the incident transmission loss TL_i. A similar procedure is used to chart transmission loss to the receiver TL_r, except that a point source at the depth of the

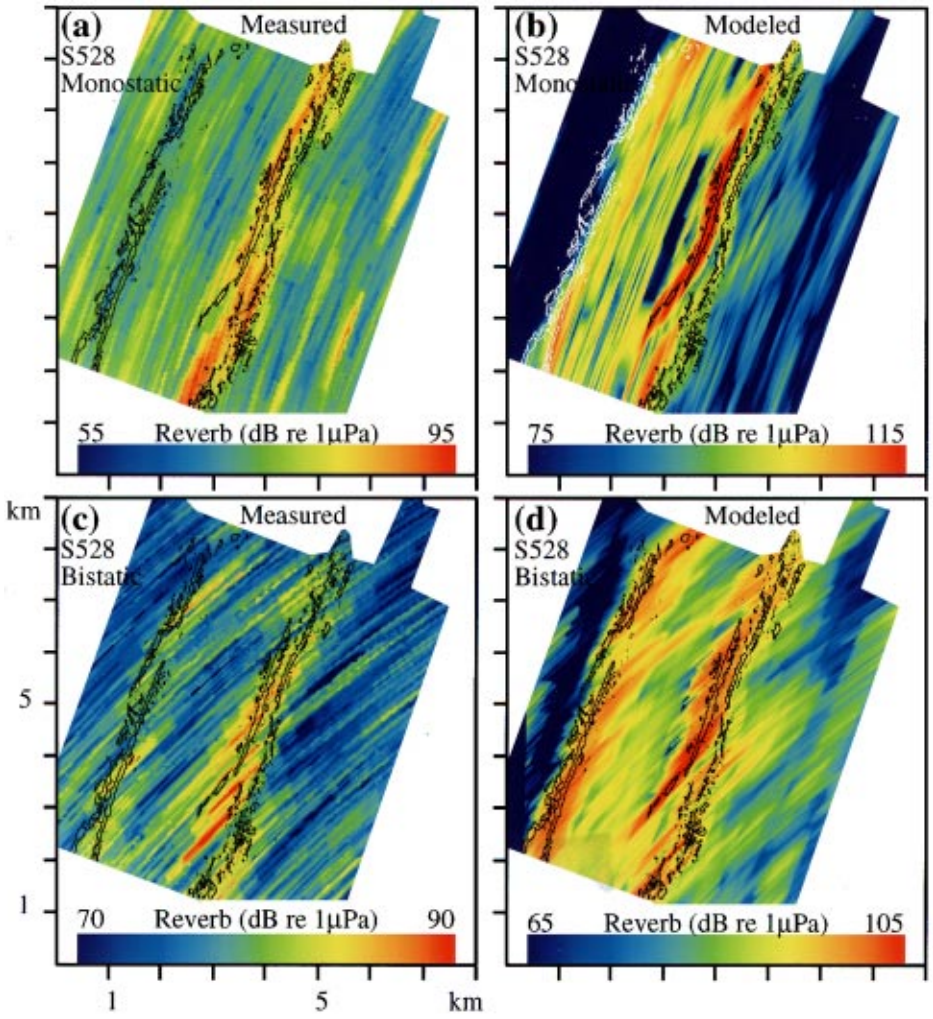

FIG. 14. High-resolution charts of monostatic and bistatic measured and modeled reverberation for S528 over the region shown in Fig. 2 with upper and lower scarp contours overlain. (a) Measured monostatic reverberation. (b) Modeled monostatic reverberation. (c) Measured bistatic reverberation. (d) Modeled bistatic reverberation.

given receiving array is used to exploit reciprocity from the scattering site. This follows the benign assumption that mean transmission loss will not vary significantly across the receiving array. The range-depth TL_r plotted in Fig. 15(b) and (c) shows less structure and leads to more uniform transmission loss back to the receiver across the region where high-resolution bathymetry is available, which lies at the 1/2 CZ vertex.

Charts of the various projection and transmission loss terms of Eq. (2), presented in Fig. 17 over the region of high-resolution bathymetry for S435, show substantial spatial structure that varies considerably from monostatic to bistatic geometries when the bistatic separation is large.

Since bathymetry within the resolution footprint of the MAE bistatic towed-array systems *cannot* be approximated as a planar surface, as demonstrated in Sec. I, Eqs. (1) and (2) cannot directly describe measured reverberation and its level. The complicated nature of bathymetry within the resolution footprint, however, leads to a simple *statistical* description of the *expected* intensity at the receiver that makes these expressions relevant. Specifically, the system resolution footprint covers an annular sector of roughly 50 m by 1000 m at 1/2 CZ, and so contains surface roughness of high complexity with respect to the mean acoustic wavelength of 6.7 m. The total field received from the footprint then behaves as the sum of a large number of statistically independent fields scattered from disjoint subregions of the resolved seafloor patch.[27] The *expected* intensity radiated from the resolution patch, proportional to the *variance* of the received field, can then be charted to the centroid of the patch by the convolution

$$\langle I(x,y|\mathbf{r}_i,\mathbf{r}_r)\rangle = \int\int_{-\infty}^{\infty} G(x-X,\ y-Y|\mathbf{r}_i,\mathbf{r}_r) \times f(\theta_i,\phi_i;\theta_r,\phi_r) \times w l_i l_r \cos\theta_i \cos\theta_r dX\, dY, \tag{3}$$

where $G(x,y|\mathbf{r}_i,\mathbf{r}_r)$ is a point-spread function[27] equal to the squared magnitude of the combined linear beam pattern and matched-filter functions that define the towed-array receiver. Here, all cosine, transmission loss, and BSDF factors are implicit functions of the spatial coordinates of the integral, and the expected intensity is a function of the source and receiver locations $\mathbf{r}_i$, $\mathbf{r}_r$, which may vary in 3-D.

The overwhelming contribution to the convolution integral typically comes from the resolution footprint $A_f(x,y|\mathbf{r}_i,\mathbf{r}_r)$ which is defined in Appendix A. This observation has been previously exploited in Refs. 28, 11, and 2, and leads to the relation

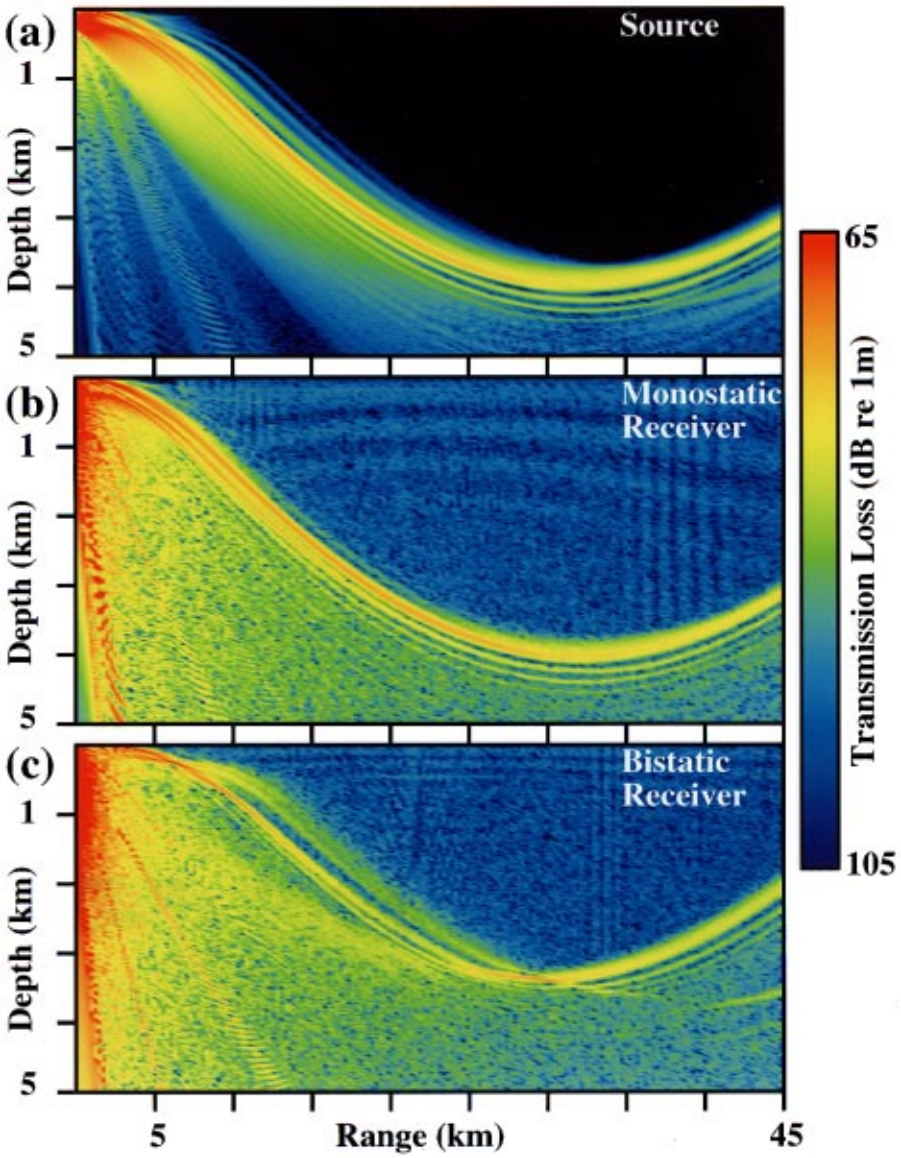

FIG. 15. (a) Range-depth slice of broadband transmission loss in the 200–255-Hz band modeled incoherently with the parabolic equation for the CORY 10-element source array, centered at 181 m depth with 2.5-m projector spacing and MAR vertical sound-speed structure (Ref. 2) in a bottomless ocean. (b) Same as (a) except source is now at a single point, at the 170-m depth of the CORY receiving array. (c) Same as (b) except source is a point at the 460-m depth of the ALLIANCE receiving array. The B' abyssal hill is typically 1/2 CZ (~33.3 km) from the source or receiver. Its peak lies at a depth of ~3500 m.

$$\langle I(x,y|\mathbf{r}_i,\mathbf{r}_r)\rangle \approx \int\int_{A_f(x,y|\mathbf{r}_i,\mathbf{r}_r)} f(\theta_i,\phi_i;\theta_r,\phi_r) w l_i l_r \cos\theta_i \cos\theta_r dX\, dY, \tag{4}$$

which is a very close approximation to Eq. (3) when sidelobe leakage is insignificant, as it is for prominent returns across a fixed travel-time ellipse. Recasting it in decibels yields

$$R_{\langle I\rangle}(x,y|\mathbf{r}_i,\mathbf{r}_r) \approx W + 10\log\left(\int\int_{A_f(x,y|\mathbf{r}_i,\mathbf{r}_r)} 10^{[F(\theta_i,\phi_i;\theta_r,\phi_r)-\mathrm{TL}_i-\mathrm{TL}_r+C_i+C_r]/10} dX\, dY\right). \tag{5}$$

The important issue here is that scattering distribution's strength F is not linearly proportional to the level of expected reverberation unless F is a constant over the resolution footprint. Constancy of F in A_f requires either it be independent of spatial position, incident, and scattered angle or the scattering surface be a plane over which F may vary with incident and scattered angle but not position. To obtain F from measured reverberation in any other case requires a deconvolution, of the kind worked out in Ref. 28 and implemented with wide-area MAE data in Ref. 2. A successful deconvolution, however, depends on a sufficient set of independent measurements[28] as well as charting error that is insignificant compared to the dimension of the seafloor patch to be resolved. While both of these conditions were satisfied in the wide-area analysis of Ref. 2, neither is met in the present analysis of high-resolution data.

Given these considerations, any estimate of seafloor scattering strength obtained in the present analysis will inevitably be blurred over the resolution footprint of the towed-array system. To describe this blurring, it is convenient to define

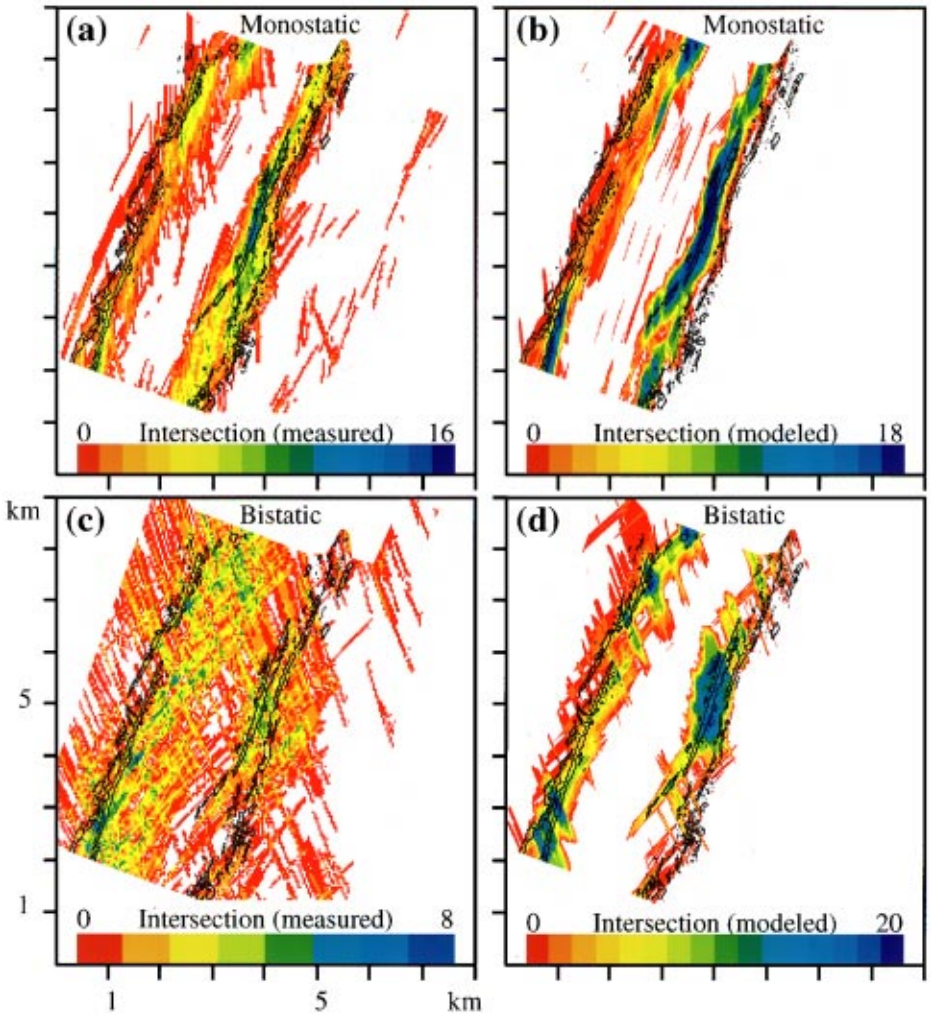

FIG. 16. Spatial distribution of the most prominent returns. The upper 5% of reverberation within the high-resolution region is selected for each segment. The overlap frequency of these selected regions is shown in (a) for monostatic measured reverberation, (b) monostatic modeled reverberation, (c) bistatic measured reverberation, and (d) bistatic modeled reverberation. Red indicates regions of zero intersection; that is, where reverberation is only in the upper 5% for a single segment. All 18 monostatic and 20 bistatic segments shown in Fig. 3 are used for this computation.

$$R_M(x,y|\mathbf{r}_i,\mathbf{r}_r)=W+10\log\left(\int\int_{A_f(x,y|\mathbf{r}_i,\mathbf{r}_r)} 10^{(-\mathrm{TL}_i-\mathrm{TL}_r+C_i+C_r)/10}dX\,dY\right), \tag{6}$$

as *modeled reverberation* from a seafloor that scatters equally in all directions. Variations in modeled reverberation then arise only as the integral of surface projection and transmission loss terms over A_f. This construction leads to a simple linear equation for the *mean* strength of the scattering distribution over the resolution footprint

$$\overline{F}(x,y|\mathbf{r}_i,\mathbf{r}_r)=R_{\langle I\rangle}(x,y|\mathbf{r}_i,\mathbf{r}_r)-R_M(x,y|\mathbf{r}_i,\mathbf{r}_r). \tag{7}$$

Note that both incident and scattered angles are integrated over the resolution footprint. Blurring is then considerable, since these angles have large standard deviations over the footprint, as shown in Sec. I.

From Eq. (7), the maximum likelihood estimate for $\overline{F}$ is

$$\hat{\overline{F}}(x,y|\mathbf{r}_i,\mathbf{r}_r)=R(x,y|\mathbf{r}_i,\mathbf{r}_r)-R_M(x,y|\mathbf{r}_i,\mathbf{r}_r), \tag{8}$$

namely, the difference between reverberation measured with MAE data $R(x,y|\mathbf{r}_i,\mathbf{r}_r)$ and $R_M(x,y|\mathbf{r}_i,\mathbf{r}_r)$ reverberation modeled with the diffuse scattering assumption $F=0$.

Under the assumption that the receiver measures a circular complex Gaussian random (CCGR) field,[2,27] reverberation measured from a given surface patch obeys the exponential-gamma distribution.[10] This follows from the central-limit theorem and the fact that the system resolution footprint is much larger than wavelength-scale surface roughness.[9,10,27] A bias-corrected estimate for $\overline{F}$ is then

$$\tilde{\overline{F}}(x,y|\mathbf{r}_i,\mathbf{r}_r)=R(x,y|\mathbf{r}_i,\mathbf{r}_r)-R_M(x,y|\mathbf{r}_i,\mathbf{r}_r)+(\psi(N)-\ln N)10\log e, \tag{9}$$

following Ref. 10 where $\psi(N)$ is Euler's psi function with measurement degrees of freedom N defined in Sec. I.

D. Comparison between measured and modeled charts of high-resolution reverberation

Charts of modeled reverberation R_M, obtained from transmission loss and surface projection maps by applying the spatial convolution described in Eq. (6), are presented in Figs. 12–14(b) and (d) for comparison with charts of measured reverberation R, in Figs. 12–14(a) and (c).

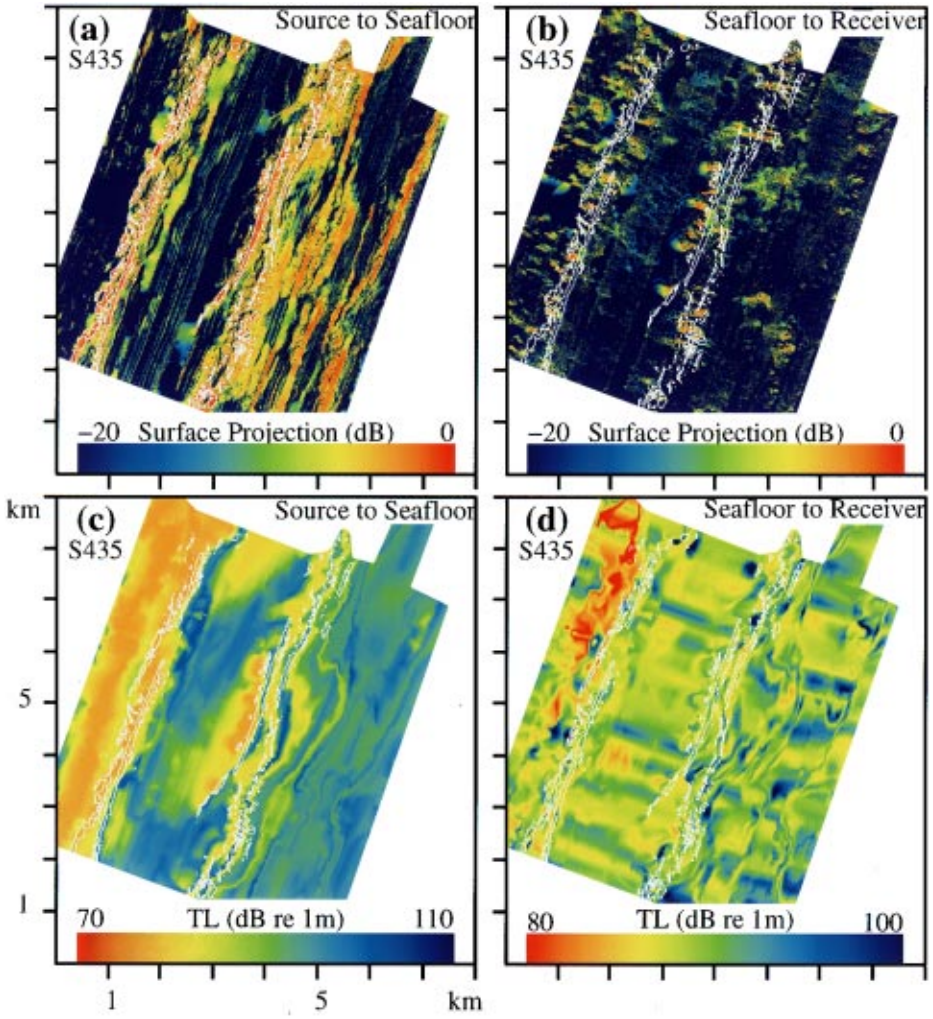

FIG. 17. Projection and transmission loss terms over the region of high-resolution bathymetry for S435 from Eq. (2). (a) Surface projection $C_i = 10\log(\cos\theta_i)$ of bathymetry from source to seafloor using raytrace. (b) Surface projection $C_r = 10\log(\cos\theta_r)$ of bathymetry from seafloor to ALLIANCE receiving array center point using raytrace. (c) Transmission loss TL_i from CORY 10-element source array to scattering patch using parabolic equation incoherently integrated from 200–255 Hz. (d) Transmission loss TL_r from seafloor to ALLIANCE receiving array center point using parabolic equation incoherently integrated from 200–255 Hz.

Measured and modeled reverberation show close qualitative agreement in all monostatic charts. The most prominent returns resolve the morphology of the upper and lower scarps with reasonable accuracy primarily because the cross-range axis of the resolution footprint typically lies along the scarp axis and so does not bleed into neighboring regions, such as the plateau and trench. Returns from these neighboring regions are typically about 20 to 30 decibels lower. Since this variation greatly exceeds the expected 2.5 to 5.6 dB standard deviation, the scarps emerge as deterministic features of the data. The measured and modeled reverberation charts also agree on when the upper scarp will fall in the shadow zone, as it does in S528.

The spatial frequency distribution of the upper 5% of modeled reverberation for the monostatic charts is shown in Fig. 16(b). The modeled distribution bears a close resemblance to the corresponding measured one, with the weight of prominent returns charted to the steepest portions of the upper and lower scarps. This result is consistent with the high visual correlation found between measured and modeled monostatic reverberation.

The situation is different for the bistatic data. While the general *character* of measured reverberation shows qualitative agreement with the modeled in all bistatic charts, the kind of high visual correlation found in the monostatic comparison only appears when the bistatic separation between source and receiver azimuths is small enough for prominent returns to faithfully image scarp morphology. More frequently, the bistatic separation is too large for this, and elliptic arcs of both measured and modeled reverberation, obliquely centered on the scarp axes, bleed into neighboring plateaus over lengths commensurate with the resolution footprint. As a result, the overall reverberation level in the vicinity of the scarps is much higher than in neighboring regions where no scarps are present, as is often more clearly seen in the wide-area charts of Sec. II A. This level fluctuates drastically along the scarp, in both measured and modeled charts, with an inner scale equaling the range resolution of the system. The most prominent *modeled* returns typically coincide with a characteristic nonlinearity of the scarp, such as a canyon wall, that projects area strongly along the acoustic path from source to scatterer to receiver for the given bistatic geometry. The separation between these large projections is typically much greater than the range resolution of the system, but shorter than the cross-range resolution. This is consistent with the greater uniformity in level found in monostatic reverberation images of the scarps, where many canyons are blurred together in cross-range.

The most prominent *measured* returns often do not coincide with the most prominent *modeled* returns when the bistatic separation is large, although they are all typically centered somewhere along the upper or lower scarp. To il-

lustrate this point, the expected spatial frequency distribution of the highest 5% of modeled bistatic reverberation is shown in Fig. 16(d). As in the monostatic case, prominent returns are most frequently charted to steep regions of the scarps in both the measured and modeled distributions. The measured distribution, however, differs significantly from the modeled one in that it shows a relatively high frequency of prominent returns charted to the plateau region between the two scarps, while a relatively small number are expected there according to the model. There are two plausible explanations for these inconsistencies. First, the model predicts variations in reverberation level along the scarp that are on the order of the 5.6-dB maximum standard deviation expected in the data. This type of signal-dependent noise, conventionally referred to as *speckle*,[10,25,27,28] is then sufficient to bury the pattern predicted by the model.[2] Second, there may be charting errors that exceed the range-resolution of the system. This is extremely plausible because fluctuations in receiver array heading in excess of 0.1° are sufficient to cause such errors at 1/2 CZ. Moreover, fluctuations of this order were often observed during reception of any given LFM by the ALLIANCE. The second explanation is consistent with an overall rotation of predicted reverberation and is consistent with off-scarp charting of prominent returns, but does not account for the apparent randomization bistatic returns along the scarp as does the presence of speckle noise.

III. BI-AZIMUTHAL SCATTERING FROM THE B' ABYSSAL HILL

A. Site-specific approach

The development of Sec. II C makes clear that it is typically not possible to estimate the BSDF of the B' abyssal hill directly from MAE data. Only the *mean* BSDF, or equivalently the strength of the mean scattering distribution over a resolution footprint, can be estimated. But, this central value is not necessarily independent of the method of measurement. To minimize the effects of the measurement and to make sense of the bidirectional scattering properties contained in reverberation charts, some further reduction of the data is necessary. The approach behind this reduction becomes clearer when the following four points are considered.

First, the seafloor within a resolution footprint of the towed-array imaging system cannot be approximated as a planar surface, except perhaps within the plateau region. Therefore, we find it senseless to plot estimates of scattering strength as a function of mean incident and scattered angle over the resolution footprint, and instead take another approach.

Second, the source and receiver locations for each transmission can be uniquely identified by the receiver azimuth which spans a full half-space about B', whereas the source azimuth is restricted to values near zero. It is both convenient and natural then to plot measured reverberation, modeled reverberation and estimated scattering strength as a function of receiver azimuth with respect to the B' axis, with the understanding that the full bi-azimuthal description can be easily regained by translation through Figs. 3 and 4. For example, an estimate of the mean strength of the scattering distribution $\hat{\tilde{F}}(x,y|\mathbf{r}_i,\mathbf{r}_r)$ can be equivalently written as $\hat{\tilde{F}}(x,y|\Omega_i,\Omega_r)$, for source and receiver azimuths Ω_i, Ω_r defined with respect to the upper or lower scarp since there is a unique Ω_i, Ω_r pair for every $\mathbf{r}_i$, $\mathbf{r}_r$ pair.

Third, the geomorphology of B' is not homogeneous, but may be naturally segmented into three distinct regions. These are the upper scarp, the lower scarp, and the plateau defined in Sec. I. The results of Secs. II B–D indicate that the upper and lower scarps return the strongest echoes[2] because they direct the largest projected areas along the acoustic path from source to receiver. The plateaus, on the other hand, scatter relatively weakly and uniformly since both incident and scattered waves intersect their surfaces at extremely shallow grazing in the present long-range experiment. This is evident in both the measured and modeled reverberation of Secs. II B–D when the cross-range axis of the system resolution footprint is along the scarp axis. When the bistatic separation is large enough that the cross-range axis of the resolution footprint runs across the scarp axis, however, returns from the scarps are often falsely charted to the plateau as described in Secs. I and II, and sidelobe leakage from the scarps often contaminates true returns from the plateau which are much weaker. These effects prevent accurate determination of the bi-azimuthal scattering properties of the *plateau* when the bistatic separation is large.

Fourth, measured reverberation, modeled reverberation, and the estimated strength of the scattering distribution undergo spatial fluctuations within these regions due to changes in geomorphology and the interference structure of the received field, as demonstrated in the reverberation charts of the previous section.

Our approach, in light of these points, is to arrive at a single mean strength for the bi-azimuthal scattering distribution across the upper scarp of the B' abyssal hill and a similar mean strength for the lower scarp. This is done by taking the average of $\hat{\tilde{F}}(x,y|\Omega_i,\Omega_r)$ with respect to x,y over each scarp and plotting the result, along with its standard deviation, as a function of receiver azimuth Ω_r with the understanding that this also specifies the source azimuth. For example, the average of some function $\Psi(x,y)$ over area A is

$$\langle \Psi(x,y)\rangle_A = \frac{1}{A}\int\int_A \Psi(x,y)\,dx\,dy, \tag{10}$$

so that its standard deviation is

$$\sigma_A\{\Psi(x,y)\} = \mathrm{sqrt}(\langle \Psi(x,y)^2\rangle_A - \langle \Psi(x,y)\rangle_A^2). \tag{11}$$

Since the average value $\langle \hat{\tilde{F}}(x,y|\Omega_i,\Omega_r)\rangle_A$ is over a large region A comprising either the upper or lower scarp, and F is independent of local seafloor foreshortening, its use (1) circumvents difficulties regarding the use of scattering strength to characterize nonplanar and poorly resolved scattering surfaces, (2) is consistent with a natural segmentation of seafloor geomorphology, (3) smooths over spatial fluctuations, and (4) remains highly relevant to long-range waterborne measurements since these generally entail the kind of near-

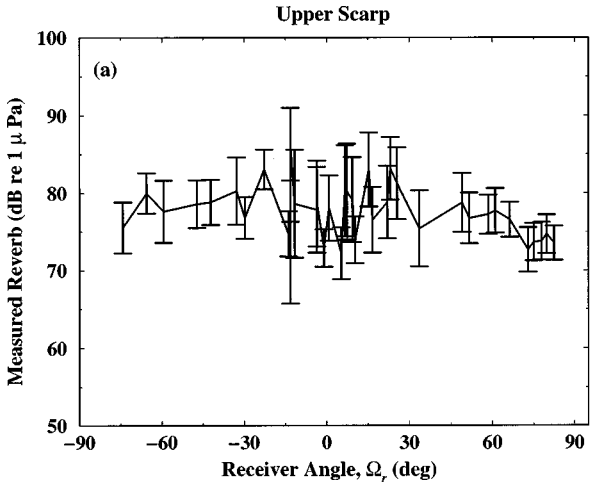

FIG. 18. The mean reverberation level measured over (a) the upper scarp $\langle R(x,y|\Omega_i,\Omega_r)\rangle_{A_{\rm up}}$ and (b) the lower scarp $\langle R(x,y|\Omega_i,\Omega_r)\rangle_{A_{\rm low}}$ as a function of receiver azimuth Ω_r with respective standard deviations $\sigma_{A_{\rm up}}\{R(x,y)\}$ and $\sigma_{A_{\rm low}}\{R(x,y)\}$.

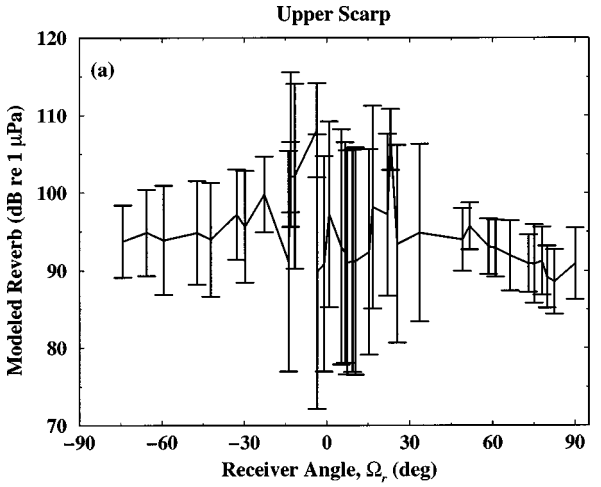

FIG. 19. The mean reverberation level modeled over (a) the upper scarp $\langle R_M(x,y|\Omega_i,\Omega_r)\rangle_{A_{\rm up}}$ and (b) the lower scarp $\langle R_M(x,y|\Omega_i,\Omega_r)\rangle_{A_{\rm low}}$ as a function of receiver azimuth Ω_r with respective standard deviations $\sigma_{A_{\rm up}}\{R_M(x,y)\}$ and $\sigma_{A_{\rm low}}\{R_M(x,y)\}$.

horizontal propagation to and from the seafloor inherent in MAE. An information-conserving alternative to the average that has all of these properties, but is far less wieldy, is presented in Appendix B.

B. Azimuthal dependence of measured and modeled reverberation from the upper and lower scarps

Curves of mean reverberation level, measured over the upper scarp $\langle R(x,y|\Omega_i,\Omega_r)\rangle_{A_{\rm up}}$ and lower scarp $\langle R(x,y|\Omega_i,\Omega_r)\rangle_{A_{\rm low}}$, are plotted as a function of Ω_r in Fig. 18(a) and (b) along with their corresponding standard deviations $\sigma_{A_{\rm up}}\{R(x,y)\}$, $\sigma_{A_{\rm low}}\{R(x,y)\}$. These summarize the azimuthal dependence of reverberation from geomorphological features on the B' abyssal hill that stand out in remote acoustic images.

The curve for the upper scarp is remarkably flat, while that for the lower scarp shows a gradual roll-off of at most 5 dB from the origin to extreme values of Ω_r. Fluctuations in the mean, however, are on the order of the standard deviation in both curves. The latter ranges from roughly 6 dB within $|\Omega_r|<30°$, to roughly 3 dB outside this range, so that the roll-off in the lower-scarp curve is barely significant.

The region of high standard deviation near the origin has a relatively straightforward explanation. This is where the monostatic data is concentrated and main beam propagation from the source to the narrow scarps is most sensitive to slight variations in range, since the cross-range axis of the resolution footprint is along the scarp axes. This same sensitivity partially explains the complete absence of a strong return from the upper scarp in S528 monostatic in Fig. 14(a) and (b). Conversely, the standard deviations decrease as $|\Omega_r|$ increases beyond 30° because the cross-range direction of the resolution footprint takes on such an oblique angle with the scarp axes that it becomes impossible for the main beam to miss either scarp. The observed standard deviations may also be partially explained by minor charting errors which would lead to much higher fluctuations for small $|\Omega_r|$, due to these same sensitivity issues.

For comparison, curves of the mean modeled reverberation level over the upper and lower scarps, $\langle R_M(x,y|\Omega_i,\Omega_r)\rangle_{A_{\rm up}}$ and $\langle R_M(x,y|\Omega_i,\Omega_r)\rangle_{A_{\rm low}}$, are plotted

as a function of receiver azimuth in Fig. 19(a) and (b) along with their corresponding standard deviations $\sigma_{A_{\rm up}}\{R_M(x,y)\}$, $\sigma_{A_{\rm low}}\{R_M(x,y)\}$. There are a number of important similarities and differences between the modeled and measured curves. For $|\Omega_r|>30°$, the standard deviations are again lower, typically near 5 dB. Within $|\Omega_r|<30°$, they increase more drastically on the upper scarp than the lower, at roughly 10 to 7 dB, primarily because the main beam of the source array is able to more consistently insonify the lower scarp for small $|\Omega_r|$. While the modeled mean across the upper scarp has a relatively flat dependence on receiver azimuth, in accord with the measured mean, the modeled mean across the lower scarp has an unambiguously convex dependence, peaking within $|\Omega_r|<30°$ and rolling off by roughly 10 dB as $|\Omega_r|$ approaches 90°.

An explanation for this behavior requires analysis of the projection and TL terms before convolution. The mean two-way transmission loss $\langle \mathrm{TL}_i(x,y|\Omega_i,\Omega_r)+\mathrm{TL}_r(x,y|\Omega_i,\Omega_r)\rangle_{A_{\rm up}}$, $\langle \mathrm{TL}_i(x,y|\Omega_i,\Omega_r)+\mathrm{TL}_r(x,y|\Omega_i,\Omega_r)\rangle_{A_{\rm low}}$ and mean surface projection $\langle C_i(x,y|\Omega_i,\Omega_r)+C_r(x,y|\Omega_i,\Omega_r)\rangle_{A_{\rm up}}$, $\langle C_i(x,y|\Omega_i,\Omega_r)+C_r(x,y|\Omega_i,\Omega_r)\rangle_{A_{\rm low}}$ over the upper and lower scarps are plotted as a function of receiver azimuth for this purpose in Figs. 20 and 21, along with their standard deviations.

The mean surface projection curves show very regular convex behavior with remarkably small standard deviation. At the extreme values of $|\Omega_r|$, however, levels are only about 5 dB down from the peak value which lies near the origin. Since this gradual roll-off falls within the standard deviation and mean fluctuations of the two-way transmission-loss curves, which typically exceed 10 dB, it is lost in the noise when the projection and TL terms are combined. As a result, mean modeled reverberation exhibits a relatively constant overall dependence on receiver azimuth, in accord with the measured mean. Extreme fluctuations in two-way TL arise because the upper scarp falls in the shadow zone of the main beam's refractive path, for some segments such as S528, due to its proximity to the source array's conjugate depth. Since the lower scarp lies much deeper, both the standard deviation and fluctuations in the mean are small enough that a clear convex dependence arises in the mean negative two-way transmission loss that reinforces the mean surface projection trend. This leads to an unambiguous central peak in mean modeled reverberation level across the lower scarp that may also be reflected in the measured curve. The central minimum in mean two-way transmission loss across the lower scarp arises because the main beam of the source array insonifies the lower scarp most uniformly when the propagation path runs across the scarp axes. The relatively small standard deviations found in curves of mean modeled and measured reverberation level, compared with those of two-way TL, follow from the smoothing effects of spatial convolution with the system resolution footprint.

The implication of this decomposition is that *spatial variations in transmission loss and projected area lead to the dominant spatial variations in measured reverberation at long range*. This finding for *high-resolution bistatic* data is entirely consistent with that of the previous *wide-area* analyses of *monostatic* data,[2,11] where the effect of projected surface area was incorporated implicitly in range-dependent propagation modeling via the parabolic equation.

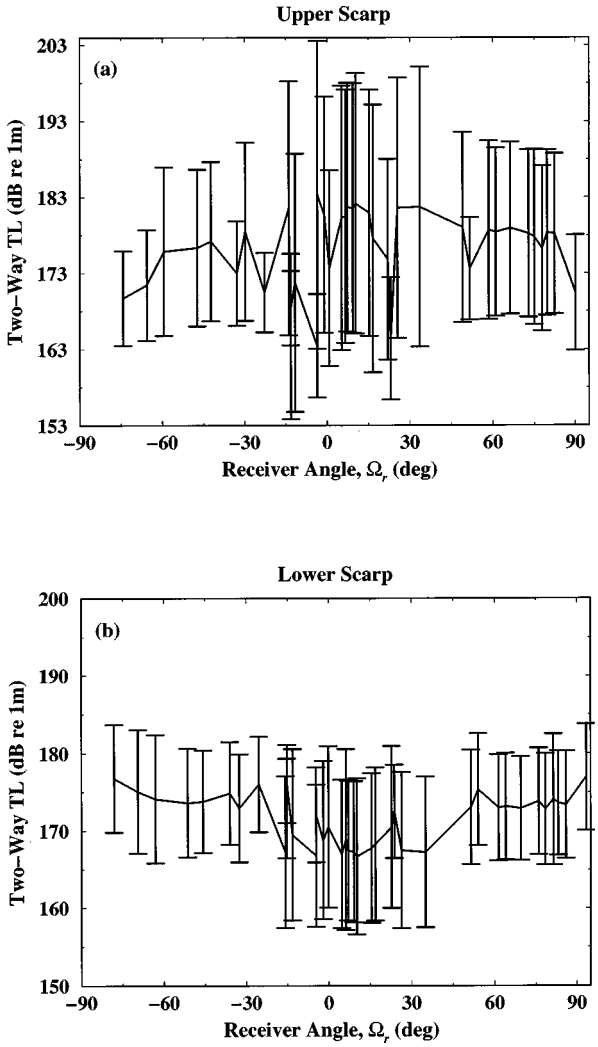

FIG. 20. The mean two-way transmission loss (a) over the upper scarp $\langle \mathrm{TL}_i(x,y|\Omega_i,\Omega_r)+\mathrm{TL}_r(x,y|\Omega_i,\Omega_r)\rangle_{A_{\rm up}}$ and (b) lower scarp $\langle \mathrm{TL}_i(x,y|\Omega_i,\Omega_r)+\mathrm{TL}_r(x,y|\Omega_i,\Omega_r)\rangle_{A_{\rm low}}$ as a function of receiver azimuth Ω_r along with standard deviations.

C. Bi-azimuthal scattering distribution of upper and lower scarps

Curves of the mean strength of the bi-azimuthal scattering distribution over the upper scarp $\langle \hat{\tilde{F}}(x,y|\Omega_i,\Omega_r)\rangle_{A_{\rm up}}$ and lower scarp $\langle \hat{\tilde{F}}(x,y|\Omega_i,\Omega_r)\rangle_{A_{\rm low}}$ are plotted as a function of receiver azimuth in Fig. 22, along with their corresponding standard deviations $\sigma_{A_{\rm up}}\{\hat{\tilde{F}}(x,y)\}$, $\sigma_{A_{\rm low}}\{\hat{\tilde{F}}(x,y)\}$. The mean strength over the upper scarp fluctuates about a constant value of roughly $-17\,\mathrm{dB}\pm 8\,\mathrm{dB}$. The larger standard deviation and fluctuations in the mean for small $|\Omega_r|$ are consistent with those found in both curves of measured and modeled reverberation level. While one may argue that a very mild concave trend is displayed in the mean scattering

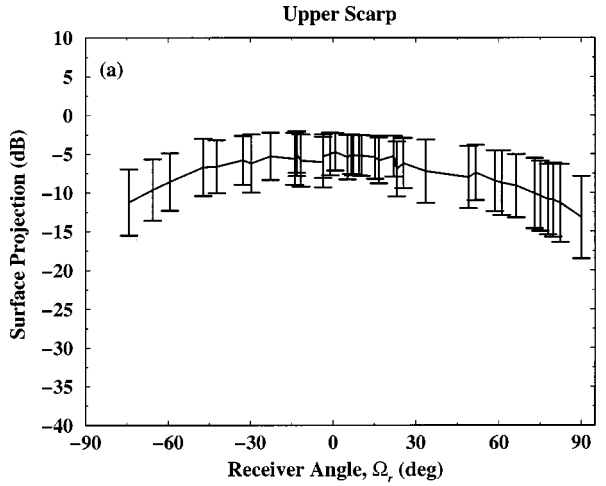

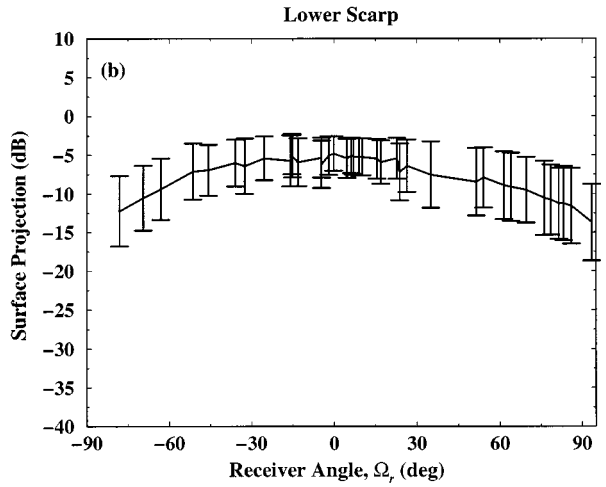

FIG. 21. The mean surface projection, in dB, (a) over the upper scarp $\langle C_i(x,y|\Omega_i,\Omega_r)+C_r(x,y|\Omega_i,\Omega_r)\rangle_{A_{\rm up}}$ and (b) the lower scarp $\langle C_i(x,y|\Omega_i,\Omega_r)+C_r(x,y|\Omega_i,\Omega_r)\rangle_{A_{\rm low}}$ as a function of receiver azimuth Ω_r along with standard deviations.

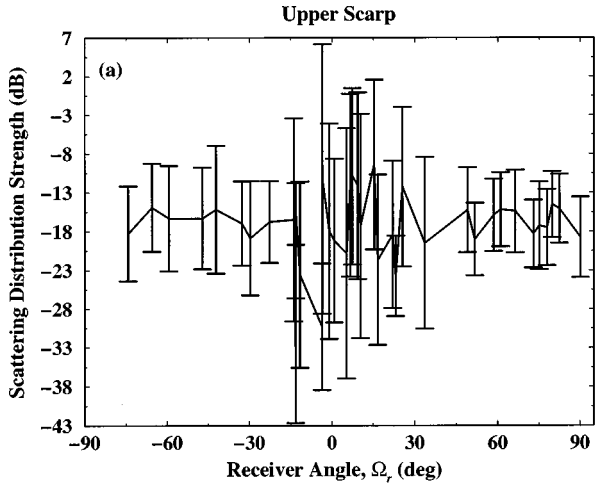

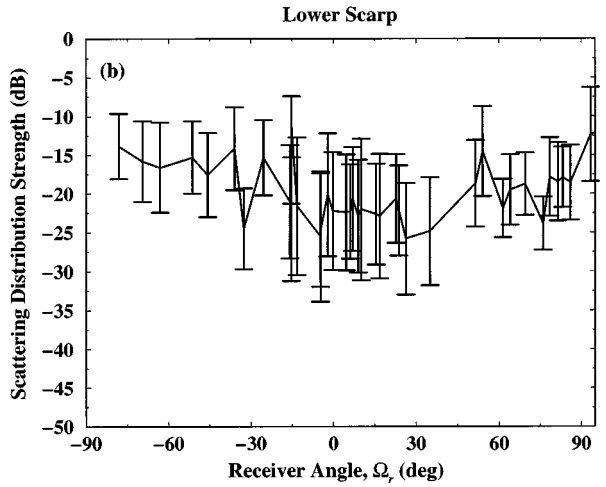

FIG. 22. The mean strength of the bi-azimuthal scattering distribution estimated over (a) the upper scarp $\langle \hat{\hat{F}}(x,y|\Omega_i,\Omega_r)\rangle_{A_{\rm up}}$ and (b) the lower scarp $\langle \hat{\hat{F}}(x,y|\Omega_i,\Omega_r)\rangle_{A_{\rm low}}$ as a function of receiver azimuth Ω_r along with the corresponding standard deviations $\sigma_{A_{\rm up}}\{\hat{\hat{F}}(x,y)\}$, $\sigma_{A_{\rm low}}\{\hat{\hat{F}}(x,y)\}$. The mean strength over the scarps fluctuates about a constant value of roughly -17 dB$\pm$8 dB.

strength curve for the lower scarp, this entire trend falls within the roughly 7-dB standard deviation shown. The far more important fact is that a constant line may be drawn across -17 dB that falls within all error bars. By reciprocity, these results remain the same if the source and receiver azimuths are interchanged.

In light of the data and our present analysis, we conclude that the *mean bi-azimuthal scattering distributions of the upper and lower scarps of the B′ abyssal hill are identical and have strengths roughly equal to the constant* -17 dB$\pm$8 dB. Whether the observed constancy is due to innate properties of the seafloor, or is a consequence of the large and nonplanar areas integrated by the resolution footprint of the towed-array system, is not particularly relevant to the type of remote sensing undertaken in the present study. The important issue is that the scarps *behave* as if their innate BSDF is spatially homogeneous and equal to the constant $10^{-1.7}$ when remotely imaged from waterborne paths at 1/2 CZ range or greater.

IV. CONCLUSIONS

High-resolution images of a typical mid-ocean abyssal hill, called B', are formed from acoustic measurements made remotely with a bistatic towed-array system at 1/2 convergence zone range. For comparison, modeled images are generated from high-resolution supporting bathymetry, sampled at the wavelength scale, with a combination of parabolic equation and ray approximations, under the assumption that the seafloor scatters uniformly in all directions. Narrow scarps, $\sim$100 m wide, that stretch along the ridge axis for kilometers, consistently produce the most prominent features in both measured and modeled images. Measured and modeled images show close agreement when the cross-range axis of the system resolution footprint is aligned with the scarp axis. In this case, prominent measured and modeled returns faithfully image scarp morphology while neighboring plateaus produce comparatively negligible returns. This is true

even though the scarps and plateaus typically share similar two-way transmission loss and exactly the same *modeled* scattering strength.

A primary conclusion can be drawn from this that could not be drawn in previous studies that relied upon lower resolution supporting bathymetry.[2,11–14] *Scarps return the strongest echoes because they project the largest area along the acoustic path from the source to receiver.* Scattering strength differences between the scarps and plateaus, arising from their differing material properties, are apparently of secondary importance in modeling long-range acoustic reverberation, which averages over large inhomogeneous seafloor areas, since a good first-order match between measured and modeled reverberation is obtained when these differences are neglected.

When the system's cross-range axis forms an oblique angle with the scarp axis, prominent returns are still centered on the scarps but also cross into neighboring plateaus over lengths commensurate with the resolution footprint's cross-range extent. Prominent *modeled* returns in this scenario typically coincide with characteristic anomalies on the scarps, such as canyon walls 100–200 m wide, that project area strongly along the acoustic path from source to receiver and lie at spatial minima in two-way transmission loss to the seafloor. While the *character* of prominent *measured* returns is similar to this, a one-to-one correspondence with *modeled* returns is absent at these oblique angles. The most likely explanation for this discrepancy is that the expected pattern along the scarp is lost in signal-dependent noise arising from statistical fluctuations of the scattered field. Specifically, the along-scarp variations in reverberation level predicted by the model are on the order of the 5.6-dB standard deviation expected in the scattered field by the central-limit theorem. While there is also some evidence of charting error, introduced by undersampled fluctuations in receiving-array orientation, this leads to rotational offsets in the images as opposed to the observed randomization.

This result can be cast in more general terms. *Signal-dependent noise, commonly referred to as speckle, is one of the primary factors limiting a towed-array imaging system's ability to remotely resolve seafloor geomorphology.* Degradation is most pronounced when the expected reverberation level has spatial variations that do not greatly exceed the 5.6-dB standard deviation of speckle noise, as is the case when the terrain to be imaged is relatively uniform, even if this means that it is uniformly rough as is the case along the B' scarps.

Both measured and modeled reverberation share the same nearly constant bi-azimuthal dependence, when averaged across either scarp of the B' abyssal hill. As a result, *the mean bi-azimuthal scattering distributions of the two major scarps on the B' abyssal hill are identical and have strengths roughly equal to the constant* $-17\,\mathrm{dB}\pm 8\,\mathrm{dB}$. Whether or not this constancy describes an innate property of the scarps that remains unchanged in more localized and high-resolution measurements is not relevant to the type of remote sensing undertaken in the present study. The important issue here is that the scarps *behave* as if their innate bi-azimuthal scattering distribution function is spatially homogeneous and equal to the constant $10^{-1.7}$ when remotely imaged from waterborne paths at $1/2+n$ CZ range. From these ranges, in other words, the scarps behave as Lambertian scatterers with albedo $\pi/10^{1.7}$.

This result for the B' abyssal hill leads to a more general hypothesis. *Spatial variations in transmission loss and seafloor projected area cause the dominant spatial variations in the expected value of long-range ocean-basin reverberation.* This hypothesis is appealing because it means that long-range reverberation from the ocean basin can be adequately modeled given two environmental inputs: (1) the refractive index of the water column, and (2) bathymetry. The latter must be of sufficient resolution to determine the projected area of primary seafloor scatterers. Research is presently directed to test this hypothesis by analyzing the bi-azimuthal scattering properties of an *inside corner*. The results of this research will be important because inside corners, and *outside corners* like the B' abyssal hill, comprise the two major geological classes of bathymetric highs in the world's mid-ocean ridges.[29]

APPENDIX A: THE RESOLUTION FOOTPRINT

The resolution footprint $A_f(x,y|\mathbf{r}_i,\mathbf{r}_r)$ can be described without loss of generality in a simple 2-D Cartesian coordinate system shown in Fig. A1, where the receiver $\mathbf{r}_r$ is at the origin and the source $\mathbf{r}_i$ on the y-axis at positive a. The travel-time radius from the source is $r_a=\sqrt{x^2+(y-a)^2}$ and that from the receiver is r. An ellipse of constant two-way travel time can be defined by holding $R=r_a+r$ fixed. Points on the ellipse are naturally described by polar coordinates with respect to the receiver location $x=r\cos\theta$ and y

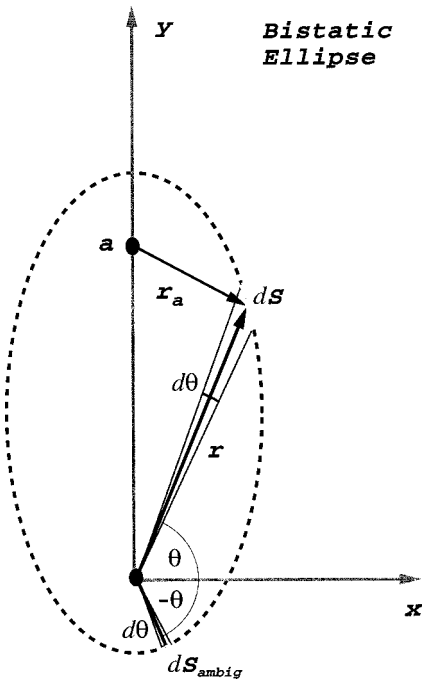

FIG. A1. Elliptical geometry of a bistatic measurement with a true feature at (r,θ). The receiving array lies along the x-axis and is centered at the origin so that the ambiguous azimuth is $-\theta$. If the receiving array has azimuthal resolution $b(\theta)=d\theta$, the system's cross-range resolution is dS, with an ambiguity of arc-length dS_{ambig} as shown.

$=r\sin\theta$ so that the azimuthal resolution of the receiving array is set to $\beta(\theta)=d\theta$, the range resolution to roughly dr, and the cross-range resolution to

$$ds=\sqrt{r^2+\left(\frac{\partial r}{\partial\theta}\right)^2}\,d\theta,$$

where

$$\frac{\partial r}{\partial\theta}=\frac{ra\cos\theta}{R-a\sin\theta}.$$

The resolution footprint in this coordinate system is then

$$A_f=dr\,ds=\sqrt{r^2+\left(\frac{ra\cos\theta}{R-a\sin\theta}\right)^2}\,dr\,d\theta.$$

The cross-range resolution ds then reduces to $rd\theta$ for monostatic geometries, while for general bistatic measurements in the present semicircular experimental geometry about B' it is roughly bounded by $\sqrt{3/2}rd\theta\approx 1.2rd\theta$ since the source–receiver separation a never exceeds r.

Minor perturbations in this elliptic geometry arise when travel time range is converted to actual spatial range, due to the combined effects of vertical refraction and bathymetric variation.

APPENDIX B: INFORMATION-CONSERVING SUMMARY OF THE BI-AZIMUTHAL SCATTERING DISTRIBUTION OF THE UPPER AND LOWER SCARPS

The mean reverberation and scattering distribution strength curves shown in Figs. 18, 19, and 22 only summarize the relevant data without loss of information[30] when the samples from which the means are extracted are Gaussian variates. This, however, is not the case with the present data, so an information-conserving summary of the azimuthal scattering distribution of the upper and lower scarps is presented in Figs. B1–B3. Here, histograms of measured reverberation, modeled reverberation, and scattering strength,

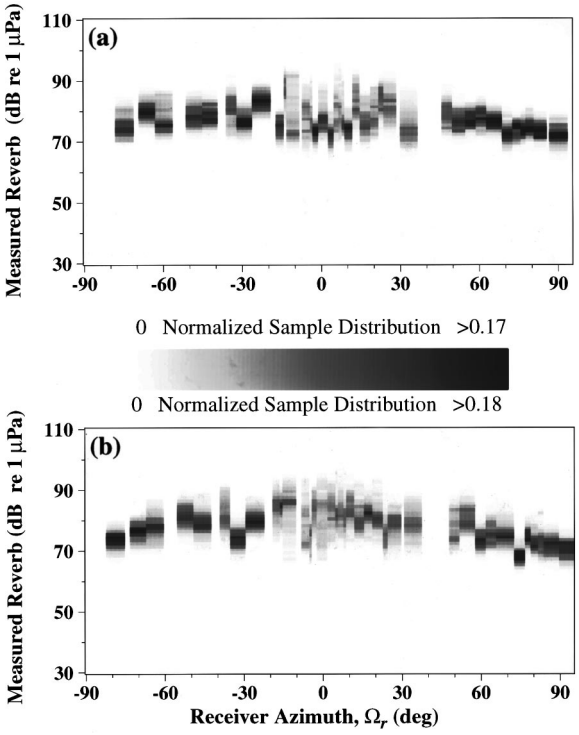

FIG. B1. Histogram of measured reverberation level over (a) the upper scarp and (b) the lower scarp as a function of receiver azimuth Ω_r.

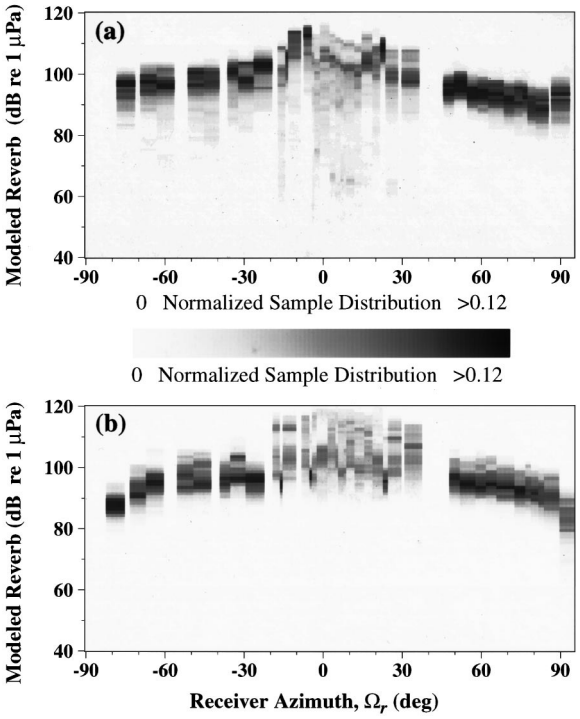

FIG. B2. Histogram of modeled reverberation level over (a) the upper scarp and (b) the lower scarp as a function of receiver azimuth Ω_r.

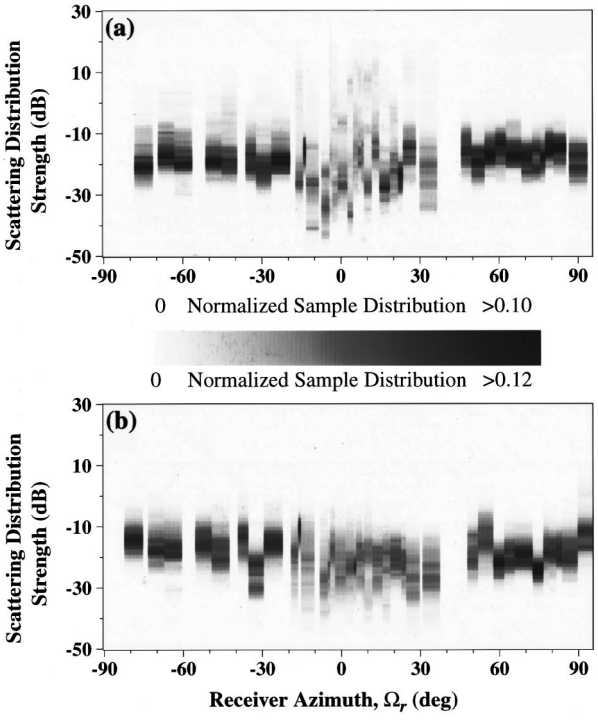

FIG. B3. Histogram of scattering distribution strength over (a) the upper scarp and (b) the lower scarp as a function of receiver azimuth Ω_r.

with samples taken over the upper and lower scarps, respectively, are given as a function of receiver azimuth.

[1] *Acoustic Reverberation Special Research Program Main Acoustics Experiment, Initial Report*, edited by J. Orcutt, Scripps Institution of Oceanography (1993).

[2] N. C. Makris, L. Z. Avelino, and R. Menis, ''Deterministic reverberation from ocean ridges,'' J. Acoust. Soc. Am. **97**, 3547–3574 (1995). [Bathymetry in Fig. 5 of this reference should be labeled <3600 m not <3200 m as shown. Also, the bistatic reverb for LFM/S478 should be labeled >87 dB *re* 1 μPa in Fig. 24, not >80 dB *re* 1 μPa as shown.]

[3] B. E. Tucholke, W. K. Stewart, and M. C. Kleinrock, ''Long-term denudation of ocean crust in the central North Atlantic Ocean,'' Geology **25**, 171–174 (1997).

[4] E. Gerjouy and A. Yaspan, ''Reverberation,'' in *The Physics of Sound in the Sea* (National Defense Research Committee, Washington, DC, 1946).

[5] N. C. Makris, ''Proposed experiment,'' in *Acoustic Reverberation Special Research Program Research Symposium*, Woods Hole Oceanographic Institution (1992).

[6] N. C. Makris and B. Gardner, ''Planned Tracks/Waypoints, Runs 3–9,'' in *Acoustic Reverberation Special Research Program Main Acoustics Experiment, Initial Report*, Scripps Institution of Oceanography (1993), pp. 65–80.

[7] B. E. Tucholke, J. Lin, M. C. Kleinrock, M. A. Tivey, T. B. Reed, J. Goff, and G. E. Jaroslow, ''Segmentation and crustal structure of the western Mid-Atlantic Ridge flank, 25° 25′–27°10′N and 0–29 m.y.,'' J. Geophys. Res. **102**, 10 (1997); **102**, 203–210 (1997); **102**, 223 (1997).

[8] J. R. Preston, E. Michelozzi, L. Troiano, and R. Hollet, ''Cruise report on RV ALLIANCE cruise MARE 5 July–1 August 1993 SACLANTCEN's joint experiment with ONR's ARSRP Group,'' SACLANT Undersea Research Centre, LaSpezia, Italy (1993).

[9] P. Swerling, ''Probability of detection for fluctuating targets,'' Rand Report RM 1217 (1954); reissued in Trans. IRE Prof. Group Inf. Theory **IT-6**, 269–308 (1960).

[10] N. C. Makris, ''The effect of saturated transmission scintillation on ocean acoustic intensity measurements,'' J. Acoust. Soc. Am. **100**, 769–783 (1996).

[11] N. C. Makris and J. M. Berkson, ''Long-range backscatter from the Mid-Atlantic Ridge,'' J. Acoust. Soc. Am. **95**, 1865–1881 (1994).

[12] N. C. Makris, L. Avelino, R. Menis, and J. M. Berkson, ''Preliminary results: Correlation between reverberation and geomorphology,'' in *Acoustic Reverberation Special Research Program Main Acoustics Experiment, Initial Report*, Scripps Institution of Oceanography (1993), pp. 336–355.

[13] K. B. Smith, W. S. Hodgkiss, and F. D. Tappert, ''Propagation and analytic issues in the prediction of long-range reverberation,'' J. Acoust. Soc. Am. **99**, 1387–1404 (1996).

[14] A. J. Harding, M. A. H. Hedlin, and J. A. Orcutt, ''Migration of backscatter data from the Mid-Atlantic Ridge,'' J. Acoust. Soc. Am. **103**, 1787–1803 (1998).

[15] D. M. Fromm, L. B. Palmer, and J. P. Crockett, ''Bi-RASP: The bistatic range-dependent active system prediction model,'' Technical Report NRL/FR/7140-95-9723 (Naval Research Laboratory, Washington D.C., 1996).

[16] V. Lupien, ''The importance of scale structure in scattering from random rough surfaces,'' Ph.D. thesis, Massachusetts Institute of Technology, Cambridge, MA, 1998.

[17] ''Positioning with GPS-1985,'' in *Proceedings First International Symposium on Precise Positioning with the Global Positioning System*, Vol. 1, C. C. Goad, Covenor, National Geodetic Information Center (NOAA, Rockville, Maryland, 1985).

[18] J. P. Snyder, ''Map projections—A working manual,'' USGS Professional Paper 1395 (1985).

[19] G. I. Evenden, ''Cartographic Projection Procedures for the Unix Environment—A user's manual,'' USGS Open-File Report 90-284 (1991).

[20] B. K. P. Horn and R. W. Sjoberg, ''Calculating the reflectance map,'' Appl. Opt. **18**, 1770–1779 (1979).

[21] F. E. Nicodemus, J. C. Richmond, J. J. Hsia, I. W. Ginsbrg, and T. Limperis, ''Geometrical considerations and nomenclature for reflectance,'' NBS Monograph 160 (National Bureau of Standards, Washington, D.C., October 1977).

[22] Readers must be warned that the Nicodemus *et al.* (Ref. 21) and Horn and Sjoberg references (Ref. 20) use the term *radiant intensity* to mean flux per unit solid angle, by a convention in modern radiometry. This differs from the term *intensity* used in field theory that means flux per unit area. Also, the BSDF here is equivalent to the bidirectional reflectance distribution function (BRDF) of modern radiometry, except inverse steradians units are stressed in the latter but not the former. The distinction, with no real difference, arises because the nondimensional steradian unit cannot be readily conserved in the relation $dA = r^2\, d\Omega$ between differential area dA and differential solid angle $d\Omega$. The term *scattering* is preferred here over *reflectance*, since the two are not equivalent in field theory.

[23] R. Urick, *Principles of Underwater Sound*, 3rd ed. (Peninsula, Los Altos, CA, 1983), pp. 274–278.

[24] S. Chandrasekhar, *Radiative Transfer* (Dover, New York, 1960).

[25] N. C. Makris, ''A foundation for logarithmic measures of fluctuating intensity in pattern recognition,'' Opt. Lett. **20**, 2012–2014 (1995).

[26] M. D. Collins, ''A self-starter for the parabolic equation method,'' J. Acoust. Soc. Am. **92**, 2069–2074 (1992).

[27] J. W. Goodman, *Statistical Optics* (Wiley, New York, 1985).

[28] N. C. Makris, ''Imaging ocean-basin reverberation via inversion,'' J. Acoust. Soc. Am. **94**, 983–993 (1993).

[29] B. E. Tucholke and J. Lin, ''A geological model for the structure of ridge segments in slow spreading ocean crust,'' J. Geophys. Res. **99**, 11937–11958 (1994).

[30] P. M. Woodward, *Probability and Information Theory with Applications to Radar* (Pergamon, Oxford, England, 1953).